



HAL
open science

Modeling Extinction and Reddening Effects by Circumstellar Dust in the Betelgeuse Envelope in the Presence of Radiative Torque Disruption

Bao Truong, Le Ngoc Tram, Thiem Hoang, Nguyen Chau Giang, Pham Ngoc Diep, Dieu D. Nguyen, Nguyen Thi Phuong, Thuong D. Hoang, Nguyen Bich Ngoc, Nguyen Fuda, et al.

► **To cite this version:**

Bao Truong, Le Ngoc Tram, Thiem Hoang, Nguyen Chau Giang, Pham Ngoc Diep, et al.. Modeling Extinction and Reddening Effects by Circumstellar Dust in the Betelgeuse Envelope in the Presence of Radiative Torque Disruption. *The Astrophysical Journal*, 2022, 936, 10.3847/1538-4357/ac86d9 . insu-03777333

HAL Id: insu-03777333

<https://insu.hal.science/insu-03777333v1>

Submitted on 12 Apr 2023

HAL is a multi-disciplinary open access archive for the deposit and dissemination of scientific research documents, whether they are published or not. The documents may come from teaching and research institutions in France or abroad, or from public or private research centers.




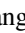


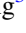
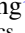
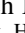
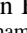

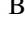
L'archive ouverte pluridisciplinaire **HAL**, est destinée au dépôt et à la diffusion de documents scientifiques de niveau recherche, publiés ou non, émanant des établissements d'enseignement et de recherche français ou étrangers, des laboratoires publics ou privés.



Distributed under a Creative Commons Attribution 4.0 International License



Modeling Extinction and Reddening Effects by Circumstellar Dust in the Betelgeuse Envelope in the Presence of Radiative Torque Disruption

Bao Truong^{1,2} , Le Ngoc Tram^{3,4} , Thiem Hoang^{5,6} , Nguyen Chau Giang^{5,6} , Pham Ngoc Diep⁷ , Dieu D. Nguyen⁸ , Nguyen Thi Phuong^{5,7} , Thuong D. Hoang^{9,10} , Nguyen Bich Ngoc^{7,11} , Nguyen Fuda^{1,2} , Hien Phan⁹ , and Tuan Van Bui⁹ 

¹Department of Physics, International University, Ho Chi Minh City, Vietnam; truonglegiabao@gmail.com

²Vietnam National University, Ho Chi Minh City, Vietnam

³Max-Planck-Institut für Radioastronomie, Auf dem Hügel 69, D-53121, Bonn, Germany; nle@mpifr-bonn.mpg.de

⁴Stratospheric Observatory for Infrared Astronomy, Universities Space Research Association, NASA Ames Research Center, MS 232-11, Moffett Field, 94035 CA, USA

⁵Korea Astronomy and Space Science Institute, 776 Daedeokdae-ro, Yuseong-gu, Daejeon 34055, Republic of Korea; thiemhoang@kasi.re.kr

⁶Korea University of Science and Technology, 217 Gajeong-ro, Yuseong-gu, Daejeon 34113, Republic of Korea

⁷Department of Astrophysics, Vietnam National Space Center, Vietnam Academy of Science and Technology, 18 Hoang Quoc Viet, Hanoi, Vietnam

⁸Université de Lyon 1, Ens de Lyon, CNRS, Centre de Recherche Astrophysique de Lyon (CRAL) UMR5574, F-69230 Saint-Genis-Laval, France

⁹University of Science and Technology of Hanoi, Vietnam Academy of Science and Technology, 18 Hoang Quoc Viet, Hanoi, Vietnam

¹⁰Kavli Institute for the Physics and Mathematics of the Universe, The University of Tokyo, 5-1-5 Kashiwanoha, Kashiwa, Chiba, 277-8583, Japan

¹¹Graduate University of Science and Technology, Vietnam Academy of Science and Technology, 18 Hoang Quoc Viet, Hanoi, Vietnam

Received 2021 November 2; revised 2022 June 16; accepted 2022 July 25; published 2022 September 6

Abstract

Circumstellar dust forms and evolves within the envelope of evolved stars, including asymptotic giant branch (AGB) and red supergiant (RSG) stars. The extinction of stellar light by circumstellar dust is vital for interpreting RSG/AGB observations and determining high-mass RSG progenitors of core-collapse supernovae. However, circumstellar dust properties are not well understood. Modern understanding of dust evolution suggests that intense stellar radiation can radically change dust properties across the circumstellar envelope through the Radiative Torque Disruption (RAT-D) mechanism. In this paper, we study the impacts of RAT-D on the grain size distribution (GSD) of circumstellar dust and model its effects on photometric observations of α Orionis (Betelgeuse). Due to the RAT-D effects, large grains formed in the dust formation zone are disrupted into smaller species of size $a < 0.5 \mu\text{m}$. Using the GSD constrained by the RAT-D effects, we model the visual extinction of background stars and Betelgeuse. We find that the extinction decreases at near-UV, optical, and IR wavelengths while increasing at far-UV wavelengths. The resulting flux potentially reproduces the observation from the near-UV to the near-IR range. Our results can be used to explain dust extinction and photometric observations of other RSG/AGB stars.

Unified Astronomy Thesaurus concepts: Red supergiant stars (1375); Circumstellar dust (236); Circumstellar envelopes (237); Circumstellar matter (241); Extinction (505)

1. Introduction

When helium burning in stellar cores is turned on, stars with initial masses of $12 M_{\odot}$ – $30 M_{\odot}$ evolve into red supergiants (hereafter RSGs; see Levesque et al. 2006 for a review). RSG stars experience significant stellar activity such as global pulsation (Goldberg 1984; Heger et al. 1997; Guo & Li 2002; Kiss et al. 2006) and large convection cells (Schwarzschild 1975; Antia et al. 1984; Fadeyev 2012; Ren & Jiang 2020), leading to the loss of materials through the stellar winds. Heavy elements are synthesized in the core until they reach Fe fusion. Due to its maximum binding energy per nucleon, Fe fusion is impossible, and the fusion core can no longer be sufficient to support against its gravity. Hence, the RSGs implode and end their lives as core-collapse supernovae (CCSNe). Chemical elements heavier than iron and cosmic dust are formed in the ejecta, which enriches the chemical abundance of the interstellar medium (ISM) (see Tielens et al. 2005 and De Beck et al. 2019 for reviews). Therefore, RSG research is essential for understanding dust formation and stellar feedback in the

ISM. Moreover, RSG studies have had substantial impact on determining the initial mass of supernova (SN) progenitors, which relates to the physical properties of SNe and their remnants.

However, observations have revealed that not all CCSN progenitors are coincident with RSGs. Smartt et al. (2009) indicated the link between RSGs and CCSNe through observations of 20 Type IIP SN progenitors, and showed an upper-limit mass of $16.5 M_{\odot}$, which is below the maximum estimated RSG mass of $25 M_{\odot}$ for CCSNe (Meynet & Maeder 2003). Several explanations have been proposed, including the loss of the H envelope through stellar pulsation (Yoon & Cantiello 2010), the creation of “failed SNe” that directly collapse to stellar-mass black holes (Woosley & Heger 2012; Lovegrove & Woosley 2013), and the limit mass of RSGs of $20 M_{\odot}$ in stellar evolution (Groh et al. 2013).

Recent studies have shown that circumstellar dust may be responsible for the missing of high-mass RSG progenitors. Circumstellar dust obscures stellar photons and produces an additional extinction, causing the underestimation of stellar luminosity, which is linked to failed searches for high-mass RSG progenitors (Smartt et al. 2009; Kochanek et al. 2012; Walmswell & Eldridge 2012; Kilpatrick & Foley 2018). Another significant impact of circumstellar dust is reddening



Original content from this work may be used under the terms of the [Creative Commons Attribution 4.0 licence](https://creativecommons.org/licenses/by/4.0/). Any further distribution of this work must maintain attribution to the author(s) and the title of the work, journal citation and DOI.

effects at short wavelengths. Circumstellar dust absorbs and scatters incoming stellar photons in UV–optical and near-IR (NIR) wavelengths, resulting in strong continuum absorption in the RSG/asymptotic giant branch (AGB) spectra (Massey et al. 2005; Fonfría et al. 2020; Fonfría et al. 2021). Thus, studying circumstellar dust in RSGs and their extinction properties may help resolve the RSG problems and identify high-mass RSG progenitors.

Among dust properties, the grain size distribution (GSD) and its optical properties are essential parameters for determining dust extinction and stellar reddening. The first study of GSD through UV extinction by Seab & Snow (1989) reported a lower cutoff of the GSD at $0.08 \mu\text{m}$ due to grain shattering. The study of dust condensation in RSGs by Verhoelst et al. (2009) and in the RSG progenitor of SN 2012aw by Kochanek et al. (2012) adopted a standard Mathis–Rumpl–Nordsieck size distribution of the ISM with $dn/da \propto a^{-3.5}$ for $0.005 \mu\text{m} < a < 0.25 \mu\text{m}$ (Mathis et al. 1977). van Loon et al. (2005) adopted a single size of $0.1 \mu\text{m}$ for their study. From RSG dusty envelopes observed in IR spectra, several modelings have proposed the presence of larger grains $a > 0.1 \mu\text{m}$. Groenewegen et al. (2009) found grains with $1 \mu\text{m}$ sizes in O-rich RSGs, while Scicluna et al. (2015) investigated the maximum grain size of $0.5 \mu\text{m}$ in RSG stellar winds.

The properties of dust are modified during its formation and evolution within the circumstellar envelope (CSE). Dust grains are first formed by gas nucleation in the formation zone of $\sim 3\text{--}10 R_*$ (Cherchneff 2013). Subsequently, they can grow by gas accretion and grain–grain collisions in the inner envelope (Verhoelst et al. 2006). When dust is expelled by radiation pressure into the ISM, its properties can also be affected by radiative and mechanical feedback. In general, dust grains can be destroyed by thermal sublimation, grain shattering, and sputtering (Dominik et al. 1989; Biscaro & Cherchneff 2016). Nevertheless, thermal sublimation is inefficient in AGB/RSG cases, because dust temperature is below the sublimation threshold of 1500 K starting from the formation zone. Moreover, shattering and sputtering are only efficient in shocks when dust is injected into the ISM.

Recently, Hoang et al. (2019) introduced a new mechanism of grain disruption based on radiative torques (RATs), which is termed RAdiative Torque Disruption (RAT-D). The RAT-D mechanism can be effective in radiation fields in which thermal sublimation is insufficient. The mechanism implies that large grains spun up by RATs to fast rotation can be fragmented by centrifugal stress into smaller particles, including nanoparticles (i.e., $a < 100 \text{Å}$). Tram et al. (2020) first studied the RAT-D effect for AGB envelopes and modeled electric dipole emission from rapidly spinning nanoparticles using the GSD constrained by RAT-D. The authors demonstrated that the model within a proper GSD can explain the observations of both carbon-rich and oxygen-rich AGB stars (see their Figure 10). Therefore, the approach based on the RAT-D mechanism is plausible in determining the proper GSD and materials in the CSE of evolved stars.

In this work, we will apply RAT-D for RSG envelopes and discuss its implications for a particular star, α Orionis (Betelgeuse)—an M2 supergiant star in the end phase of evolution for high-mass stars. The star is a luminous source with a bolometric luminosity of $\sim 1.26 \times 10^5 L_\odot$ and a distance of 197 pc (see Table 1). Hence, the CSE dust grains are

Table 1
Physical Parameters of the Betelgeuse CSE

Parameters	Values	References
Distance (pc)	197 ± 45	(1)
Stellar luminosity (L_\odot)	1.26×10^5	(1)
Stellar mass (M_\odot)	19.7	(1)
Stellar radius (R_\odot)	887 ± 203	(1)
Stellar diameter (mas)	55.64 ± 0.04	(1)
Effective temperature (K)	3500 ± 200	(1), (2)
Mass-loss rate ($M_\odot \text{yr}^{-1}$)	$2 \pm 1 \times 10^{-6}$	(1), (3)
Expansion velocity (km s^{-1})	15	(3)
Inner envelope radius (R_*)	3	(3), (4)
Outer envelope radius (R_*)	17,000	(5), (6)

References: (1) Dolan et al. (2016); (2) Fay & Johnson (1973); (3) Verhoelst et al. (2006); (4) Kervella et al. (2016); (5) Noriega-Crespo et al. (1997); (6) Decin et al. (2013).

expected to be affected by the intense radiation field and their gaseous environment.

Using the GSD constrained by RAT-D, we determine the starlight absorption and scattering characteristics. We will examine the extinction properties of dust grains through modeling extinction curves along the sightline. We will demonstrate the dependency of extinction features on grain properties and the circumstellar environment. As a result, we will be able to test grain effects by reproducing the reddened spectrum in the Betelgeuse envelope.

This paper is organized as follows. Section 2 describes the physical properties of the Betelgeuse CSE. In Sections 3 and 4, we describe the principle of the RAT-D mechanism along with the procedures of modeling extinction by circumstellar dust. The modeling results, including the GSD, extinction features, and reddening effects in the stellar spectrum, are presented in Section 5. We discuss applications of the RAT-D mechanism in studying GSD in AGB/RSG envelopes and the reddening in AGB/RSG spectra and in analyzing the Betelgeuse CSE grain properties in Section 6. Finally, our main findings are summarized in Section 7.

2. Physics Model of Betelgeuse Envelope

2.1. CSE Structure

The characteristics of the Betelgeuse envelope have been studied through NIR and mid-IR observations. Verhoelst et al. (2006) revealed an excess astrosilicate emission at an inner dust shell of $20 R_*$ from mid-IR observations. The authors also showed a thin Al_2O_3 dust shell at $2\text{--}3 R_*$ above Betelgeuse, proving the scenarios of first dust condensation in the hot chromosphere. Kervella et al. (2016) resolved a dust shell at $3 R_*$ from the light scattering of Al_2O_3 dust by VLT/SPHERE/ZIMPOL. For the outer envelope, Noriega-Crespo et al. (1997) observed an arc structure at $7' \sim 17,000 R_*$ by IRAS, which was confirmed by Herschel PACS and SPIRE images (Decin et al. 2013). Decin et al. (2013) showed this outer layer is a boundary region of the Betelgeuse envelope where the circumstellar winds collide with the ISM.

Our model adopts a spherical symmetry of the dusty CSE, characterized by the observations of Noriega-Crespo et al. (1997) and Decin et al. (2013). We choose an innermost dust shell at $r_{\text{in}} = 3 R_*$ following the polarimetric results of Kervella et al. (2016), in which dust grains formed. An outermost layer

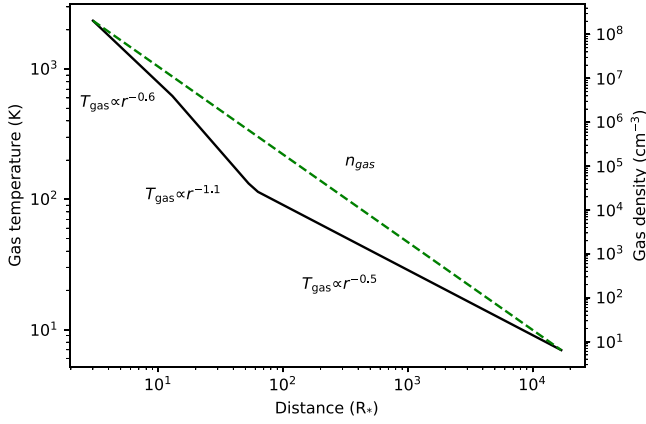


Figure 1. The mean gas density (dashed green line) and gas temperature profile (solid black line) of the Betelgeuse CSE.

is chosen at $r_{\text{out}} = 17,000 R_*$ from Noriega-Crespo et al. (1997) as we mentioned earlier. Our modeling parameters are listed in Table 1.

2.2. Gas Density Profile

Stellar activity in the photosphere produces strong shocks and ejects most of the stellar materials above an escape velocity (see Bennett 2010 for a review). The outflows accelerate until reaching a certain distance R_0 , where materials are able to condense and form the first solids. With the high flux opacity of grains, radiation pressure is sufficient to accelerate the newly formed grains and produce the drift of dust relative to the gas. This mechanism is known as radiation-driven winds (see, e.g., Höfner 2008; Höfner 2009; Höfner et al. 2016; Höfner & Olofsson 2018).

In this work, we assume that the CSE expands spherically within a constant terminal velocity v_{exp} (Tielens 1983). Hence, the gas density at a distance r is given by

$$\begin{aligned} n_{\text{gas}}(r) &= \frac{\dot{M}}{4\pi r^2 m_{\text{gas}} v_{\text{exp}}} \\ &\simeq 10^7 \left(\frac{\dot{M}}{10^{-5} M_{\odot}} \right) \left(\frac{10^{15} \text{ cm}}{r} \right)^2 \left(\frac{10 \text{ km s}^{-1}}{v_{\text{exp}}} \right) \text{ cm}^{-3} \end{aligned} \quad (1)$$

with \dot{M} denoting the mass-loss rate and $m_{\text{gas}} = 1 \text{ amu}$ denoting the hydrogen atom mass (see, e.g., Tram et al. 2020).¹² For Betelgeuse, we adopt $\dot{M} \sim 2 \times 10^{-6} M_{\odot} \text{ yr}^{-1}$ and $v_{\text{exp}} = 15 \text{ km s}^{-1}$ (Dolan et al. 2016; Verhoelst et al. 2006). The gas density profile in the Betelgeuse envelope is shown by the dashed line in Figure 1.

2.3. Gas Temperature Profile

The pressure winds transfer the gas kinetic energy into thermal energy, caused by the Alfvén wave flux, linear acoustic waves, and global pulsation (Hartmann & Avrett 1984; Pijpers & Hearn 1989; Lim et al. 1998). As a result, surrounding gas is heated to above the effective surface temperature of Betelgeuse (T_{eff} ; see, e.g., Gilliland & Dupree 1996; Lim et al. 1998).

¹² Note that the prefactor is 10^7 cm^{-3} instead of 10^6 cm^{-3} , which is a typo in Equation (1) of Tram et al. (2020), but we have checked that their gas density profile (their Figure 1) is correct.

When the gas is expanded spherically by radiation-driven winds, the temperature is balanced by the drag heating of circumstellar dust and adiabatic cooling, and drops significantly to below 100 K at the outer CSE (see, e.g., Glassgold & Huggins 1986; Rodgers & Glassgold 1991). Therefore, we construct a power-law mean gas temperature profile as follows:

$$T_{\text{gas}} = T_0 \left(\frac{r}{r_0} \right)^{-\alpha}, \quad (2)$$

where T_0 is the initial temperature and α and r_0 vary at each certain distance of the extended atmosphere. Observations and semiempirical models (Harper et al. 2001; O’Gorman et al. 2015) show that the temperature profile of the chromosphere at $2 R_* < r < 6 R_*$ drops from 3000 to 1800 K as a form of $T_{\text{gas}} \propto r^{-0.6}$. At $6 R_* < r < 60 R_*$, the temperature decreases as $T_{\text{gas}} \propto r^{-1.1}$. At a larger distance of $r > 60 R_*$, the gas temperature decreases dramatically to $\sim 6 \text{ K}$ at $r \sim 11,000 R_*$ (Rodgers & Glassgold 1991). In this stage, the temperature can be approximately $T_{\text{gas}} \propto r^{-0.5}$. The radial profile of the gas temperature is shown by the solid line in Figure 1.

3. RAT-D Mechanism and GSD

3.1. Radiation Field from an RSG Star

For a spherical envelope, the specific energy density at wavelength λ at a distance r from the central star is given by

$$u_{\lambda,0}(T_*) = \frac{\pi B(\lambda, T_*)}{c} \left(\frac{R_*}{r} \right)^2 \quad (3)$$

where T_* is the star’s effective temperature. For the sake of convenience, we consider the radiation of a central star as a blackbody, and $B(\lambda, T_*)$ follows the Planck function.

Photons emitted from the central source will be attenuated by dust extinction in the CSE. Consequently, the specific energy density is reduced to

$$u_{\lambda} = u_{\lambda,0} e^{-\tau_{\lambda}} \quad (4)$$

where $u_{\lambda,0}$ is the intrinsic energy density as shown in Equation (3), and τ_{λ} is the optical depth at wavelength λ measured from the central star.

The total energy density of the radiation field in the range of wavelengths from λ_{min} to λ_{max} is

$$u_{\text{rad}} = \int_{\lambda_{\text{min}}}^{\lambda_{\text{max}}} u_{\lambda} d\lambda. \quad (5)$$

We adopt $\lambda_{\text{min}} = 0.1 \mu\text{m}$, and $\lambda_{\text{max}} = 20 \mu\text{m}$, which cover the peak of the blackbody radiation of an RSG star with the lower limit being close to the Lyman cutoff. For convenience, we use a dimensionless parameter $U = u_{\text{rad}}/u_{\text{ISRF}}$ to refer to the strength of radiation fields with u_{ISRF} being the energy density of the average interstellar radiation field in the solar neighborhood ($u_{\text{ISRF}} = 8.64 \times 10^{-13} \text{ erg cm}^{-3}$) (Mathis et al. 1983).

Finally, the mean wavelength of the radiation field is given by

$$\bar{\lambda} = \frac{\int_{\lambda_{\text{min}}}^{\lambda_{\text{max}}} \lambda u_{\lambda} d\lambda}{\int_{\lambda_{\text{min}}}^{\lambda_{\text{max}}} u_{\lambda} d\lambda}. \quad (6)$$

For Betelgeuse, $\bar{\lambda} = 1.45 \mu\text{m}$ for an unreddened radiation field with u_{λ} given by Equation (3). This value is smaller for

the case of AGB stars, e.g., $\bar{\lambda} = 2.42 \mu\text{m}$ for IRC+10216 and $\bar{\lambda} = 2.53 \mu\text{m}$ for IK Tau (see Tram et al. 2020).

3.2. Rotational Disruption by RATs

The intense radiation field of Betelgeuse can spin up the large irregular grain shapes to an extremely fast rotation. If the induced centrifugal stress can exceed the binding energy that holds the grain constituents, the grain is spontaneously disrupted to smaller species. This destruction is called the RAT-D mechanism (see Hoang et al. 2019 and Lazarian & Hoang 2021 for details).

Here we recall the principle of the RAT-D mechanism. The maximum angular velocity that a dust grain of size a can achieve by RATs is given by

$$\omega_{\text{RAT}} = \frac{\Gamma_{\text{RAT}} \tau_{\text{damp}}}{I}, \quad (7)$$

where $I = 8\pi\rho a^5/15$ is the inertia moment of the spherical dust grain, and τ_{damp} is the total rotational damping timescale. Above, Γ_{RAT} is the RAT, which is given by (see Equation (6) in Giang & Hoang 2021)

$$\Gamma_{\text{RAT}} = \int_{\lambda_{\text{min}}}^{\lambda_{\text{max}}} \pi a^2 \gamma_{\text{rad}} u_{\lambda,0} e^{-\tau_{\lambda}} \left(\frac{\lambda}{2\pi}\right) Q_{\lambda} d\lambda \quad (8)$$

where $u_{\lambda,0}$ is given by Equation (3), and γ_{rad} is the degree of anisotropy of the radiation field. For the unidirectional radiation field from a central star, one has $\gamma_{\text{rad}} = 1$. Here, $Q_{\lambda} = \alpha(\lambda/a)^{-\eta}$ is the RAT efficiency. From numerical calculations of RATs for different shapes and orientations of dust grains (Lazarian & Hoang 2007; Hoang et al. 2021), the RAT efficiency is approximately equal to $2.33(\lambda/a)^3$ for $a < a_{\text{trans}}$ and to 0.4 for $a_{\text{trans}} < a < \lambda/0.1$, where $a_{\text{trans}} = \lambda/1.8$ is the transition grain size from the flat to the power-law RAT efficiency.

The grain rotation is slowed down by a combination of collisional damping by gas collision and the IR reemission of grains. The characteristic damping timescale is

$$\tau_{\text{damp}} = \frac{\tau_{\text{gas}}}{1 + F_{\text{IR}}}. \quad (9)$$

The corresponding characteristic timescale of collisional damping is

$$\tau_{\text{gas}} \simeq 8.74 \times 10^4 a_{-5} \hat{\rho} \left(\frac{30 \text{ cm}^{-3}}{n_{\text{H}}}\right) \left(\frac{100 \text{ K}}{T_{\text{gas}}}\right)^{1/2} \text{ yr}, \quad (10)$$

and the dimensionless IR damping coefficient is

$$F_{\text{IR}} \simeq \left(\frac{0.4U^{2/3}}{a_{-5}}\right) \left(\frac{30 \text{ cm}^{-3}}{n_{\text{H}}}\right) \left(\frac{100 \text{ K}}{T_{\text{gas}}}\right)^{1/2}, \quad (11)$$

where $a_{-5} = a/(10^{-5} \text{ cm})$ and $\hat{\rho} = \rho/(3 \text{ g cm}^{-3})$ (see Equations (12) and (13) in Tram et al. 2020). One can see from Equations (7)–(11) that the angular velocity depends on the local gas density n_{H} , gas temperature T_{gas} , and radiation strength U .

The critical angular velocity at which the grain is fragmented due to the centrifugal force is given as (see Equation (3) in

Hoang et al. 2019)

$$\omega_{\text{disr}} = \frac{2}{a} \left(\frac{S_{\text{max}}}{\rho}\right)^{1/2} \simeq 3.65 \times 10^9 a_{-5}^{-1} \hat{\rho}^{-1/2} S_{\text{max},9}^{1/2} \text{ rad s}^{-1}, \quad (12)$$

where $S_{\text{max},9} = S_{\text{max}}/(10^9 \text{ erg cm}^{-3})$ is the maximum tensile strength of grains (Hoang et al. 2019). The tensile strength is characterized by the grain internal structure. As discussed in Hoang et al. (2019), porous/composite grains have low values of $S_{\text{max}} = 10^6\text{--}10^9 \text{ erg cm}^{-3}$, whereas compact grains have higher values of $S_{\text{max}} \gtrsim 10^{10} \text{ erg cm}^{-3}$.

Consequently, the maximum grain size determined by the RAT-D mechanism (a_{disr}) is calculated numerically by setting $\omega_{\text{RAT}} \equiv \omega_{\text{disr}}$, and grains larger than a_{disr} would be disrupted.

Note that the condition of the RAT-D mechanism is valid for grains aligned at attractor points of high angular momentum (a. k.a. high- J attractors) due to the spin-up effects (see Hoang et al. 2021). These grains can experience disruption with a timescale less than that of the gas damping. For grains at low- J attractors, their angular momentum is smaller and coupled by thermal rotation of gas (denoted by J_{thermal}), and thus they are inefficiently disrupted by the RAT-D mechanism (see Hoang et al. 2021 for further explanation). The rotational disruption properties of grains have a significant impact on our calculation of the GSD, and will be discussed in the next section.

3.3. GSD

Our model assumes that the Betelgeuse envelope contains mostly O-rich dust (e.g., crystalline olivine and amorphous silicate; see Draine & Lee 1984 and Greenberg & Li 1996), which presented in spectroscopic observations taken by Verhoelst et al. (2009) and Kervella et al. (2011). The GSD follows a power law as follows:

$$\frac{dn_{\text{sil}}}{da} = C_{\text{sil}} n_{\text{H}} a^{-\alpha}, \quad (13)$$

where C_{sil} is the corresponding normalization constant of astrosilicate dust. The GSD has lower and upper cutoffs denoted by a_{min} and a_{max} , respectively.

The original dust in the dust formation zone is expected to have large size with $a_{\text{max}} > 0.25 \mu\text{m}$ (Sciicluna et al. 2015). While being expanded outward by radiation pressure, a fraction $f_{\text{high-}J}$ of original large grains at high- J attractors can achieve suprathermal rotation (i.e., $J > J_{\text{thermal}}$) and be effectively disrupted by RATs, and thus, the disruption size a_{disr} represents the upper cutoff of the GSD. The depletion of large grains and enhancement of smaller grains also modify the slope of the GSD. Meanwhile, the remaining portion $1 - f_{\text{high-}J}$ of original grains at low- J attractors rotate thermally (i.e., $J \sim J_{\text{thermal}}$). With decreased angular momentum, the RAT-D mechanism cannot occur and this results in the maintenance of the original GSD with a fixed a_{max} and $\alpha = 3.5$. As shown in Lazarian & Hoang (2021), the value of $f_{\text{high-}J}$ depends on the grains' properties and magnetic susceptibility. From the RAT calculations by Herranen et al. (2021) for an ensemble of irregular grain shapes, $f_{\text{high-}J}$ is about 10%–70% for ordinary paramagnetic materials such as astrosilicate.

For the case of grains at high- J attractors, we consider a modified GSD with a fixed normalization constant and a varying power-law index, according to model 1 in Giang et al. (2020).

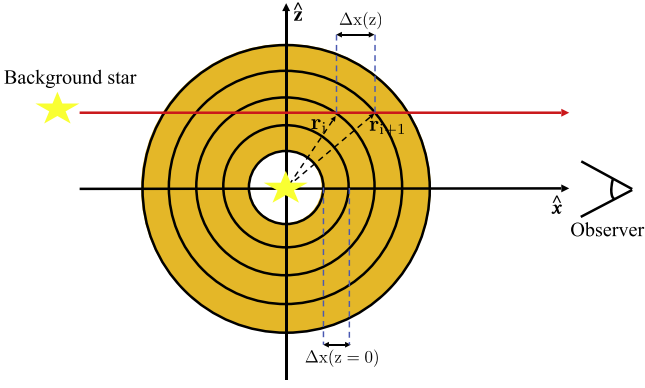


Figure 2. Schematic of radiative transfer modeling by dust grains along an LOS across the CSE in the $\hat{x}\hat{z}$ plane (middle slab with $y = 0$). The central star is considered as the origin. The positive direction of x is chosen to be directly toward the observer on Earth.

Hence, the fixed normalization constant C_{sil} is computed through the dust-to-gas mass ratio η as

$$\eta = \frac{4\pi}{m_{\text{H}}} \frac{a_{\text{max}}^{0.5} - a_{\text{min}}^{0.5}}{0.5} C_{\text{sil}} \rho_{\text{sil}}, \quad (14)$$

where $\rho_{\text{sil}} = 3.5 \text{ g cm}^{-3}$ is the mass density of silicate grains. Eventually, the modification of the power-law index is determined through the mass conservation as (see Equation (14) in Giang et al. 2020)

$$\frac{a_{\text{max}}^{0.5} - a_{\text{min}}^{0.5}}{0.5} = \frac{a_{\text{disr}}^{4+\alpha} + a_{\text{min}}^{4+\alpha}}{4 + \alpha}, \quad (15)$$

where $a_{\text{min}} = 3.5 \text{ \AA}$ is fixed, determined by the thermal sublimation of astrosilicate dust (see Draine & Salpeter 1979; Giang et al. 2020). We assume that the original dust has a maximum grain size of 0.5 \mu m . However, we also consider the effect of the variation of a_{max} from 0.05 \mu m to 0.5 \mu m .

4. Extinction Curve Modeling

4.1. Model Setup

Our work adopts a spherical geometry of the CSE within a coordinate system $\hat{x}\hat{y}\hat{z}$ having the origin at the center of Betelgeuse in units of $1 R_*$ as seen in Figure 2. The CSE is assumed to have an inner radius of $3 R_*$ and an outer radius of $17,000 R_*$. The line of sight (LOS) toward the central star is along x with $z = 0$. For numerical modeling, the envelope is divided into 1700 sublayers, and each layer has the same thickness of $\Delta x(z = 0) = 10 R_* \simeq 42.4 \text{ au}$. Within each layer, the gas and dust physical properties are uniform. We also consider the extinction of background stars behind Betelgeuse. Since the distance to Betelgeuse ($d \sim 197 \text{ pc}$; see Table 1) is much larger than its envelope, the LOS of a background star is approximately parallel to the Betelgeuse LOS with $z \neq 0$. In this case, the thickness of each slab is $\Delta x(z)$, identified by the intersection of the parallel LOS and sublayers of the envelope.

4.2. Optical Depth

For each slab i along the LOS, x , toward the observer, the optical depth $\Delta\tau_i$ at wavelength λ with thickness Δx is

calculated as

$$\begin{aligned} \Delta\tau_{\lambda,i} &= \int C_{\text{ext,sil}}^i(a) \frac{dn_i}{da} da \Delta x \\ &= C_{\text{sil}} n_{\text{H},i} \left[f_{\text{high-}J} \int_{a_{\text{min}}}^{a_{\text{disr},i}} C_{\text{ext,sil}}^i(a) a^{-\alpha} da \right. \\ &\quad \left. + (1 - f_{\text{high-}J}) \int_{a_{\text{min}}}^{a_{\text{max}}} C_{\text{ext,sil}}^i(a) a^{-3.5} da \right] \Delta x, \quad (16) \end{aligned}$$

where $C_{\text{ext,sil}}^i$ is the extinction cross section of astrosilicate grains of size a and dn_i/da is the GSD extracted from Equation (13). The optical depth is produced by two separated GSDs: the fraction $f_{\text{high-}J}$ of disrupted grains at high- J attractors in the range of $a_{\text{min}} - a_{\text{disr}}$, and $1 - f_{\text{high-}J}$ of nondisrupted grains at low- J attractors in the range of $a_{\text{min}} - a_{\text{max}}$. The value of $C_{\text{ext,sil}}^i$ is taken from Hoang et al. (2013) from photon absorption and scattering in grain surfaces, which is derived from the DDSCAT code for various grain shapes and orientations (Draine & Flatau 2012). We assume that dust grains have an oblate spheroidal shape with an axial ratio of 2.

Finally, the total optical depth at wavelength λ along the LOS is the sum of the optical depth of each slab i :

$$\tau_{\lambda} = \sum_{i=1}^n \Delta\tau_{\lambda,i}, \quad (17)$$

where i spans $i = 1$ to $i = n$ (with $n = 1700$), corresponding to the farthest and closest slabs of the LOS across the Betelgeuse envelope toward the observer, respectively.

4.3. Dust Extinction

The extinction at wavelength λ along the LOS is computed as (Hoang et al. 2013)

$$A_{\lambda} = 1.086 \tau_{\lambda} = \sum_{i=1}^n 1.086 \Delta\tau_{\lambda,i} \quad (18)$$

with the optical depth given in Equation (16). To compare with observations, we normalize the extinction curve to the visual extinction at $\lambda = 0.5448 \text{ \mu m}$ in *UBVRI* passbands (see Table 2 in the Appendix B) (Bessell 2005).

Next, we compute the total-to-selective extinction ratio, R_V , as

$$R_V = \frac{A_V}{E_{B-V}} = \frac{A_V}{A_B - A_V}, \quad (19)$$

where $E_{B-V} = A_B - A_V$ is the color excess and A_B and A_V are the extinction at the blue wavelength ($\lambda_{\text{eff}} = 0.4363 \text{ \mu m}$) and visible wavelength. The value of R_V determines the steepness of the extinction curve.

Figure 3 shows the variation of R_V with respect to the maximum grain size a_{max} , assuming $a_{\text{min}} = 3.5 \text{ \AA}$, $\alpha = 3.5$, and $C_{\text{sil}}/C_{\text{carb}} = 1.12$ (Draine & Lee 1984; Laor & Draine 1993). With a mixture of astrosilicate and carbonaceous components in ISM dust (solid green line), R_V is positively correlated with the GSD, in which lower R_V implies the enhancement of smaller grains, whereas higher R_V implies the presence of large grains in the environment (see Hirashita & Voshchinnikov 2014; Nataf et al. 2016).

The optical properties of dust materials can impact the observed R_V . In the case of only O-rich dust (solid blue line), the extinction by small astrosilicates is only affected by strong

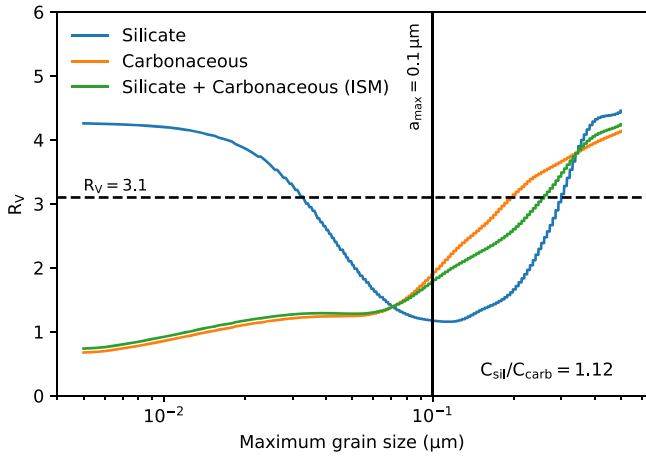


Figure 3. The calculation of the total-to-selective ratio R_V in the range of $a_{\max} = [5 \text{ nm} - 0.5 \mu\text{m}]$ of three configurations of dust: astrosilicate (blue); carbonaceous (orange); and a mixture of both dust materials (green). In the latter case, we assume a ratio between astrosilicate and carbonaceous components of $C_{\text{sil}}/C_{\text{carb}} = 1.12$.

absorption at far-UV wavelengths ($\lambda < 0.2 \mu\text{m}$) while the visible extinction is negligible (see Draine & Lee 1984 and Draine 2011 for reviews). This leads to higher R_V for smaller grains of $a < 0.1 \mu\text{m}$. For large grains of $a > 0.1 \mu\text{m}$, scattering with stellar photons becomes dominant and significantly contributes to the change in the extinction at optical wavelengths. The value of R_V starts to increase with increasing a_{\max} . The standard $R_V \simeq 3.1$ of the diffuse ISM (Cardelli et al. 1989) is possibly produced by the dominance of small astrosilicates of $a_{\max} = 0.02 \mu\text{m}$ or the abundance of large astrosilicate grains of $a_{\max} = 0.15 \mu\text{m}$, as depicted in Figure 3 (see Draine 2011). Hence, the major effects of the optical properties of O-rich compositions should be taken into consideration in the calculation of R_V .

4.4. Dust Reddening

Finally, we study the effect of dust reddening on the stellar radiation spectrum. The specific intensity of stellar radiation after being attenuated by circumstellar dust is calculated as

$$I_{\lambda} = I_{\lambda,0} e^{-\tau_{\lambda}}, \quad (20)$$

where $I_{\lambda,0} = B(\lambda, T_{*})$ is the intrinsic spectral intensity following the Planck function and $\tau_{\lambda} = A_{\lambda}/1.086$ is the optical depth derived from the dust extinction toward the central star. We study the reddened spectrum by circumstellar dust in two configurations of the GSD: the fixed GSD with the original grain sizes a_{\max} (i.e., without RAT-D), and the modified GSD with the disruption sizes a_{disr} (i.e., with RAT-D). The enhancement of smaller grain sizes in the latter is expected to increase the attenuation at UV wavelengths.

5. Numerical Results

5.1. Grain Disruption Size

Figure 4 illustrates the grain disruption size as a function of the radial distance from the central star for different values of the tensile strength and the dust-to-gas mass ratio. One can see that a_{disr} is smaller than the upper cutoff of the original GSD a_{\max} in the entire Betelgeuse envelope. Moreover, a_{disr} radially

increases with the envelope distance. The disruption size decreases with a decreasing S_{\max} or dust-to-gas ratio η .

In the framework of the RAT-D mechanism, the grain angular velocity is determined by (1) the spin-up by RATs depending on the radiation strength, and (2) the spin-down by gas collision depending on the gas density. Figure 1 shows that the gas density decreases dramatically as r^{-2} . However, the decrease rate of radiation strength is faster than that of the gas density due to the optical depth effect. Thus, the maximum grain rotation rate decreases with increasing radial distance, resulting in the increase of the disruption size. For instance, a_{disr} increases from $\sim 0.05 \mu\text{m}$ at $r = 3 R_{*}$ to $\sim 0.25 \mu\text{m}$ at $r = 17,000 R_{*}$.

The internal structure of grains also affects the efficiency of the RAT-D mechanism. A compact grain structure with higher S_{\max} is more difficult to disrupt, and the disruption size increases as $a_{\text{disr}} \propto S_{\max}^{1/4}$ (see Equation (30) in Hoang et al. 2021). For example, at $r \sim 5000 R_{*}$ within a dust-to-gas ratio of 0.002, $a_{\text{disr}} \sim 0.03$ and $0.15 \mu\text{m}$ for $S_{\max} = 10^6$ and $10^{10} \text{ erg cm}^{-3}$, respectively.

The dust-to-gas mass ratio is found to reduce the RAT-D efficiency and increase the disruption size (see Figure 4). The reason is that a higher dust-to-gas ratio corresponds to a higher amount of dust, which increases the optical depth and the attenuation of stellar radiation in the envelope. Thus, it reduces the effect of RAT-D on dust grains. As an example, for grains with $S_{\max} = 10^9 \text{ erg cm}^{-3}$ located at $r \sim 5000 R_{*}$, $a_{\text{disr}} \sim 0.06 \mu\text{m}$ with $\eta = 0.002$, but the value is $\sim 0.08 \mu\text{m}$ with $\eta = 0.01$.

Figure 5 depicts the dependency of the RAT-D efficiency on the fraction of grains at high- J attractors, denoted by $f_{\text{high-}J}$, assuming a fixed dust-to-gas ratio of $\eta = 0.01$. A higher fraction of grains at high- J attractors (i.e., higher $f_{\text{high-}J}$) are spun up and undergo a fast disruption, resulting in a smaller grain disruption size a_{disr} . Meanwhile, the higher abundance of grains at low- J attractors (i.e., lower $f_{\text{high-}J}$) requires a longer timescale to be disrupted by RATs than the gas damping time, which reduces the RAT-D efficiency and leads to a larger a_{disr} . Taking grains with $S_{\max} = 10^9 \text{ erg cm}^{-3}$ at $r \sim 5000 R_{*}$ as an example, a_{disr} decreases from ~ 0.3 to $0.2 \mu\text{m}$ with increasing $f_{\text{high-}J}$ from 50% to 100%.

Figure 6 shows the same profiles of a_{disr} , but for different values of a_{\max} , considering 50% of grains at high- J attractors. The disruption zone (in which RAT-D is effective) increases with decreasing tensile strength if $a_{\max} < 0.25 \mu\text{m}$ (top panels). For $a_{\max} = 0.1 \mu\text{m}$, as an example, the disruption zone is $r = 300 R_{*}$ for $S_{\max} \geq 10^{10} \text{ erg cm}^{-3}$ to $r = 10,000 R_{*}$ for $S_{\max} = 10^8 \text{ erg cm}^{-3}$. And for initial $a_{\max} \geq 0.25 \mu\text{m}$ (bottom panels), the disruption occurs in the entire envelope.

5.2. Extinction Curve along an LOS

We calculate the extinction curve along an LOS toward the central star of Betelgeuse ($z = 0$) and the extinction curve toward a background star ($z \neq 0$) (see Figure 2).

Figure 7 shows the normalized extinction curve, A_{λ}/A_V , at two comparable projected heights of the LOS: $z = 0$ and $z = 5000 R_{*}$. There is a strong extinction bump at $9.7 \mu\text{m}$ —the absorption feature produced by the Si–O stretching mode of astrosilicate grains. Due to the strong enhancement of smaller grains by RAT-D, the extinction curves are significantly higher at far-UV wavelengths, producing steeper slopes than in the case of no dust disruption (dashed-dotted black line).

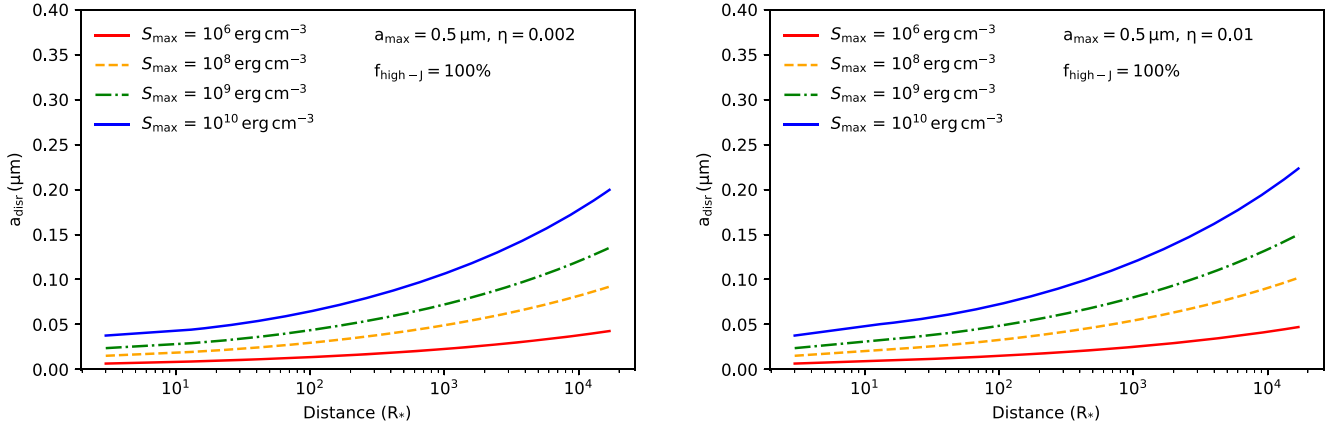


Figure 4. Disruption grain size vs. radial distance from the central star for different values of tensile strength $S_{\text{max}} = 10^6\text{--}10^{10} \text{ erg cm}^{-3}$, and for different dust-to-gas ratios $\eta = 0.002$ (left panel) and $\eta = 0.01$ (right panel), assuming the original dust has the maximum size $a_{\text{max}} = 0.5 \mu\text{m}$ and is fully disrupted by RATs ($f_{\text{high-}J} = 100\%$). Disruption is more effective for grains with lower S_{max} and lower dust-to-gas ratios.

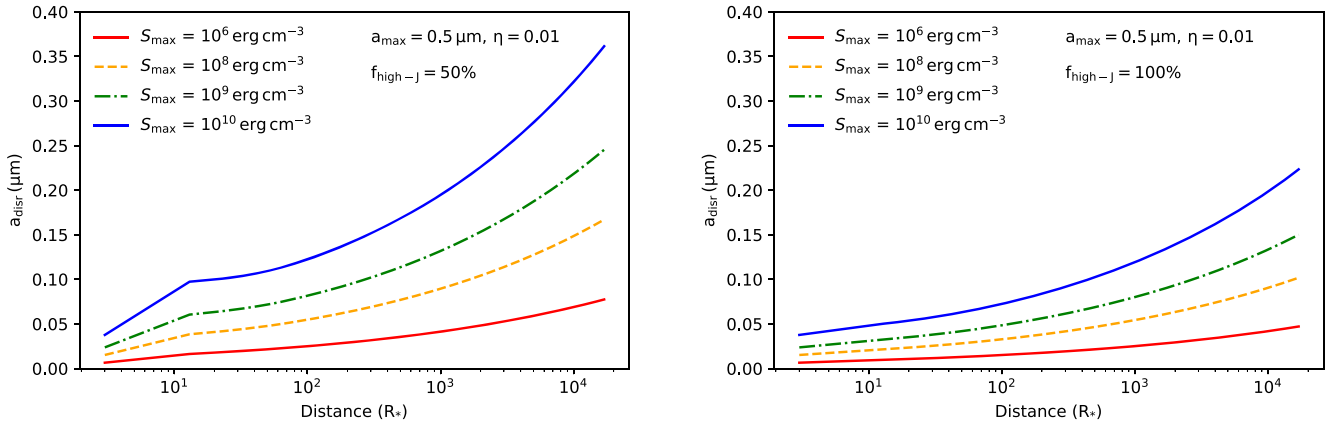


Figure 5. Same as Figure 4 but considering the effects of $f_{\text{high-}J}$ ranging from 50% (left panel) to 100% (right panel). A fixed dust-to-gas ratio of 0.01 is assumed. The RAT-D mechanism becomes more efficient when applied on grains at high- J attractors, resulting in decreased disruption grain sizes with increasing $f_{\text{high-}J}$.

Meanwhile, the extinction increases at IR wavelengths, which is a result of the normalization at the visible band ($\lambda = 0.5448 \mu\text{m}$) (see Figure 16 in the Appendix A).

The left panel of Figure 7 shows the normalized extinction curve along the LOS of $z = 0$. The slope in the UV–optical ($\lambda \sim 0.2\text{--}0.6 \mu\text{m}$) is steeper for lower values of S_{max} . It is associated with the decrease in a_{disr} with decreasing S_{max} as discussed in Section 5.1. Grains with porous structures (lower S_{max}) are more easily disrupted (smaller a_{disr}) by the RAT-D mechanism, which results in a high abundance of smaller grains. As a consequence, the extinction gets decreased at the UV–optical. In contrast, the disruption of grains with compact structures (higher S_{max}) is harder to induce, which shows a higher extinction at UV–optical wavelengths.

The right panel of Figure 7 shows the normalized extinction curves toward a background star at a projected distance $z = 5000 R_*$. The effect of small porous astrosilicate grains is more significant at the far-UV regimes, with higher extinction at lower S_{max} . Meanwhile, the IR extinction increases with decreasing S_{max} . The reason is that the disruption size in all slabs along the LOS at $z = 5000 R_*$ (see Figure 2) is larger and significantly different with varying S_{max} (see Figure 4). The discrepancy of extinction curves consequently extends from the UV–optical to the IR regimes (see Figure 16 in the Appendix A). The weaker disruption effect at lower S_{max} is unable to

increase the extinction at IR wavelengths, such that the normalization at the visible band causes an opposite order as seen in Figure 7 (right panel).

Figure 8 shows the effects of $f_{\text{high-}J}$ on the normalized extinction curves, assuming compact grains with $S_{\text{max}} = 10^9 \text{ erg cm}^{-3}$. One can see that for grains located at $z = 0$ (left panel), with lower $f_{\text{high-}J}$, fewer grains at the high- J attractor points are rapidly fragmented by RAT-D, leading to an increased population of nondisrupted large grains in the envelope and causing a decrease in far-UV extinction. Meanwhile, the normalized extinction gets increased at optical–IR wavelengths, which is a result of the increase in optical extinction for smaller $f_{\text{high-}J}$ (see Figure 17 in the Appendix A). The right panel shows similar patterns for grains located along the LOS at $z = 5000 R_*$, but with flatter curves caused by the higher abundance of large grains in this region.

Figure 9 shows the variation of extinction curves with z for grains that are fully disrupted ($f_{\text{high-}J} = 100\%$), with a fixed tensile strength of $S_{\text{max}} = 10^6 \text{ erg cm}^{-3}$ (left panel) and $S_{\text{max}} = 10^9 \text{ erg cm}^{-3}$ (right panel). The extinction is higher at far-UV regimes for lower z , which results from the enhancement of small astrosilicate grains caused by the disruption. Notably, the extinction curve at IR wavelengths is higher for smaller z with $S_{\text{max}} = 10^9 \text{ erg cm}^{-3}$, which is the opposite of the case of $S_{\text{max}} = 10^6 \text{ erg cm}^{-3}$ at UV–optical wavelengths.

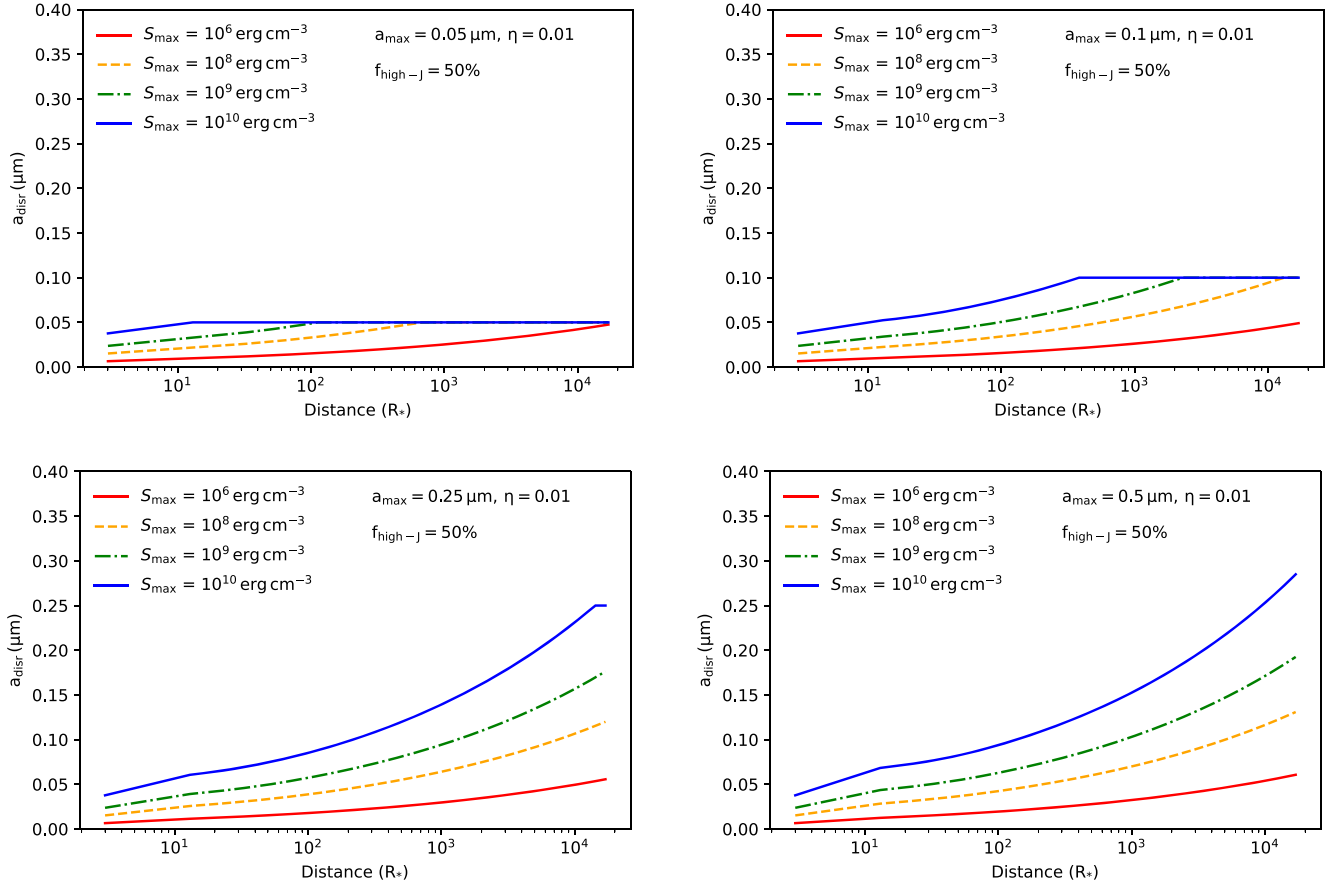


Figure 6. Same as Figure 5 but for a different initial maximum grain size a_{\max} from 0.05 to 0.5 μm , assuming a fixed $f_{\text{high-J}} = 50\%$ and $\eta = 0.01$. The disruption zone is more extended to the entire envelope as a_{\max} increases and S_{\max} decreases.

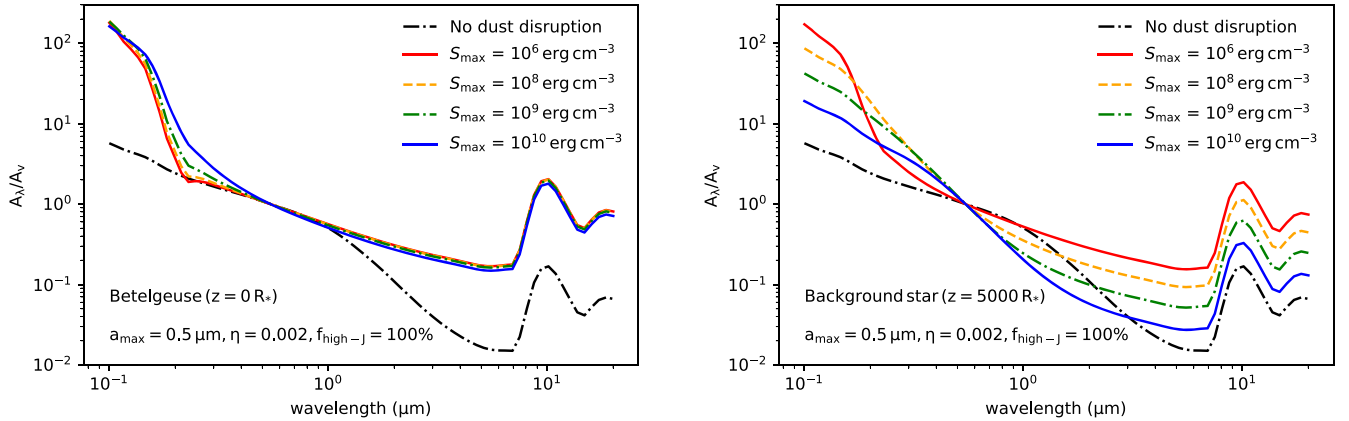


Figure 7. Extinction curve normalized by the visible extinction A_V/A_V on the LOS toward the central star, Betelgeuse ($z = 0 R_*$, left panel), and toward a background star ($z = 5000 R_*$, right panel). The original dust with $a_{\max} = 0.5 \mu\text{m}$ and $\eta = 0.002$ is adopted. Compared with the case of no dust disruption (dashed-dotted black line), the RAT-D effect results in a decrease in optical-IR extinction and an increase in far-UV extinction produced by porous grains (lower S_{\max}).

At the same height z , a porous grain is much easier to disrupt than a compact one. The extinction at optical wavelengths is less affected for grains with higher S_{\max} (see Figure 18 in the Appendix A). Thus, the normalization of the extinction curve at optical wavelengths leads to the difference in Figure 9.

Another notable difference between the left and right panels in Figures 7, 8, and 9 is that the steepness in the right panel is flatter than that in the left panel. The explanation is the total-to-

selective extinction R_V , which will be described in the next section.

5.3. Total-to-selective Extinction, R_V

As shown in the previous section, the enhancement of smaller grains decreases the dust extinction in the optical-IR wavelengths, resulting in steeper extinction curves (see

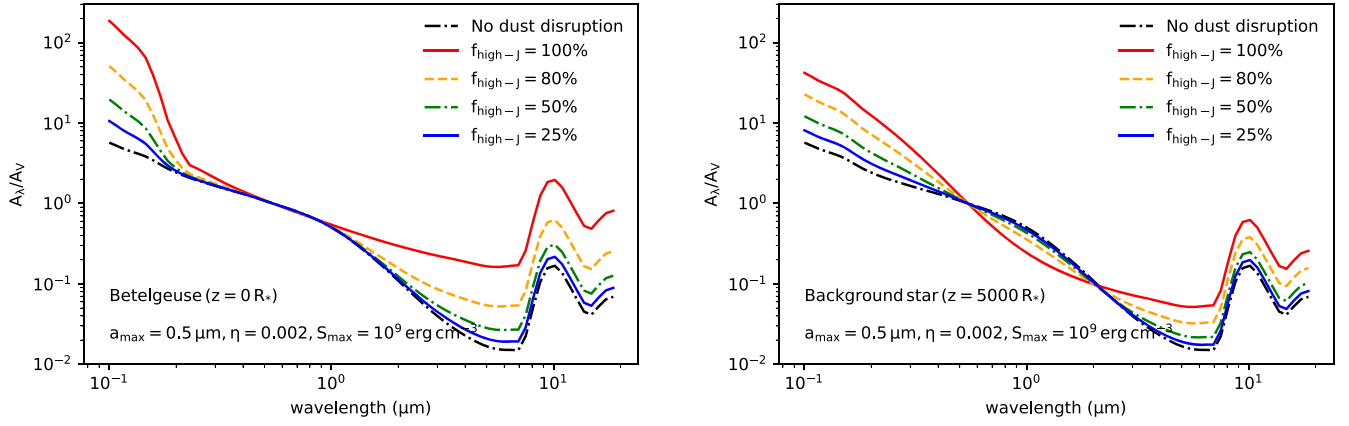


Figure 8. Same as Figure 7 but with $f_{\text{high-}J}$ ranging from 25% to 100%, assuming compact grains with $S_{\text{max}} = 10^9 \text{ erg cm}^{-3}$. The enhancement of grains at high- J attractors being disrupted by RATs causes increased far-UV extinction and decreased optical–IR extinction.

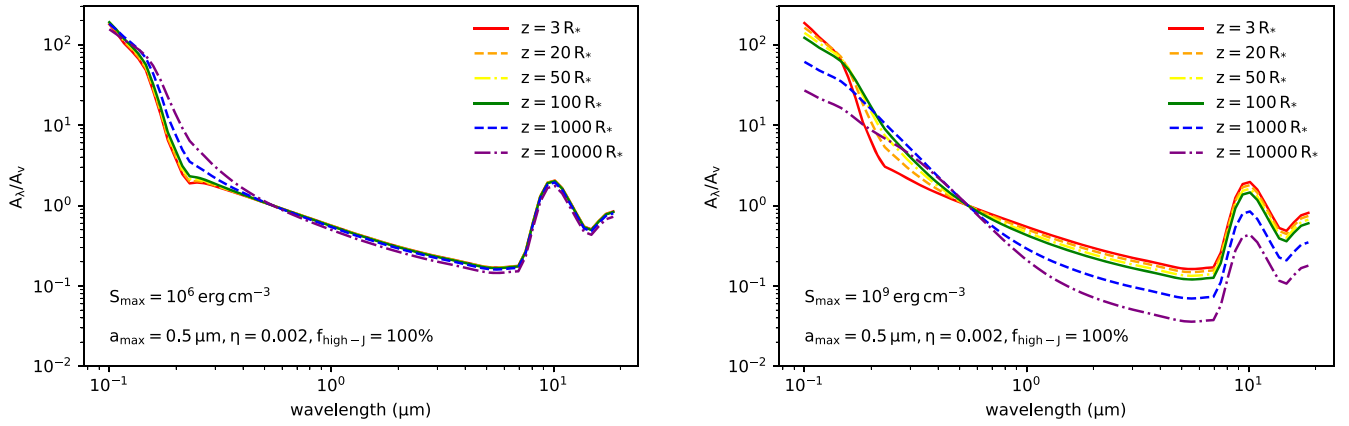


Figure 9. Same as Figure 7 but for different LOS z , assuming $S_{\text{max}} = 10^6 \text{ erg cm}^{-3}$ (left panel) and $S_{\text{max}} = 10^9 \text{ erg cm}^{-3}$ (right panel). The original dust with $a_{\text{max}} = 0.5 \mu\text{m}$, $\eta = 0.002$, and $f_{\text{high-}J} = 100\%$ is adopted. The extinction curve is steeper when observing at lower z .

Section 5.2). Additionally, the extinction patterns are affected by the optical properties of O-rich materials, resulting in different values of R_V with respect to the grain sizes as illustrated in Figure 3. In this section, we calculate the total-to-selective extinction, R_V , and show how R_V changes with the height z of the LOS.

Figure 10 shows the variation of R_V with the projected height z for different values of tensile strength and dust-to-gas ratio. Small disrupted grains of $a < a_{\text{disr}}$ cause an increase in far-UV extinction and a decrease in optical–IR extinction, leading to an observed $R_V < 4.45$ —lower than the standard value of R_V produced by the original GSD of $a < a_{\text{max}} = 0.5 \mu\text{m}$ (dashed-dotted black line).

One can see from Figure 10 that R_V increases when observing at lower positions z . This is because of the increasing effects of RAT-D toward the central star, which reduces the abundance of large grains, as shown in Figure 4. Since the major contribution of small astrosilicates of $a < 0.05 \mu\text{m}$ is only in the far-UV extinction, the extinction curve is flatter at optical–IR regimes, which results in higher R_V . Meanwhile, the increased disruption size over the envelope distance (see Figure 4) causes the enhancement of optical–IR extinction, leading to a decrease in R_V with increasing height z . The results are consistent with the features of the extinction curve along the LOS at lower z as depicted in Figure 9.

The grain internal structure plays a crucial role in the value of R_V . Close to the central star, large astrosilicate grains with lower S_{max} are fragmented into smaller sizes of $a < 0.05 \mu\text{m}$, resulting in higher R_V . Meanwhile, compact grains are hardly disrupted by RATs, leading to larger grain disruption sizes and lower values of R_V . For instance, at the height $z = 20 R_*$ within $\eta = 0.002$, R_V decreases considerably from 4.1 to 2 for grains with $S_{\text{max}} = 10^6 \text{ erg cm}^{-3}$ and $S_{\text{max}} = 10^{10} \text{ erg cm}^{-3}$. However, at the outer CSE, astrosilicate grains of $a > 0.1 \mu\text{m}$ with high tensile strength of $S_{\text{max}} > 10^9 \text{ erg cm}^{-3}$ can survive against the RAT-D mechanism and enhance the optical–IR extinction. The value of R_V increases slightly, for example at $z = 10,000 R_*$, from 1.3 for grains with $S_{\text{max}} = 10^9 \text{ erg cm}^{-3}$ to 1.8 for those with $S_{\text{max}} = 10^{10} \text{ erg cm}^{-3}$. The results are linked to the change in the slope of the observed extinction curve A_λ/A_V in Figure 7.

One contributing factor that affects R_V is the dust-to-gas mass ratio. In a low dust-to-gas ratio environment, the dust reddening effect is weaker and the RAT-D mechanism becomes more efficient. Due to the stronger disruption, the effects of the grain internal structure are more significant. As can be seen from Figure 10, the envelope with a lower dust-to-gas ratio has a higher R_V for porous grains (i.e., lower S_{max}), while the value is lower for compact grains (i.e., higher S_{max}). As an example, for grains with $S_{\text{max}} = 10^6 \text{ erg cm}^{-3}$, $R_V \sim 2.8$ as its maximum within $\eta = 0.002$ and decreases to ~ 2.4 with

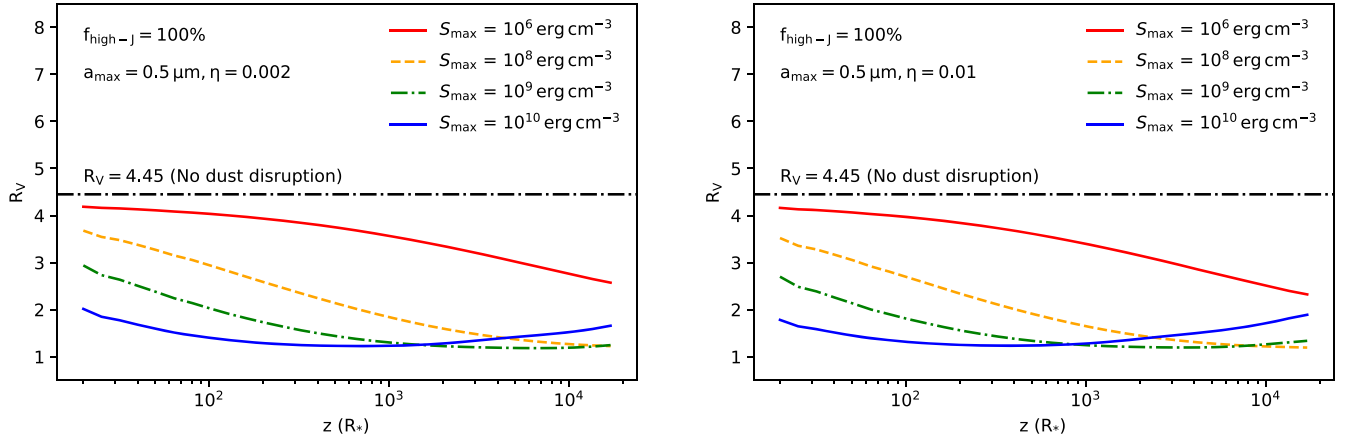


Figure 10. The change in total-to-selective ratio, R_V , over the projected height z of the LOS toward a background star, assuming different values of S_{\max} . Two dust-to-gas ratios of $\eta = 0.002$ (left panel) and $\eta = 0.01$ (right panel) are shown for a comparison. Under the effect of RAT-D, the slope of the extinction curve is steeper, resulting in lower R_V than the fixed value produced by the original dust (dashed-dotted black line). The value of R_V varies with increasing height z and tensile strength.

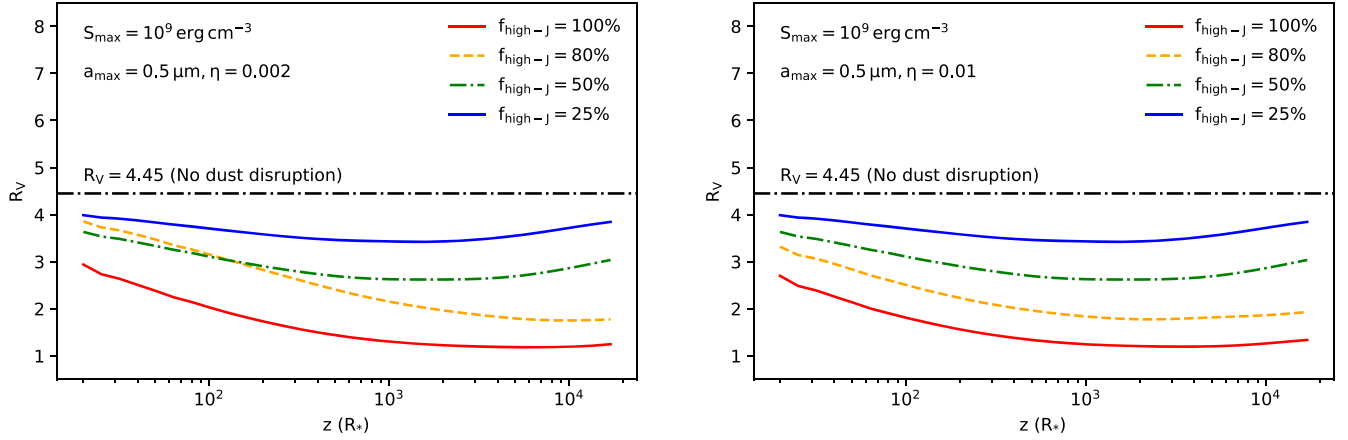


Figure 11. Same as Figure 10 but for a fixed $S_{\max} = 10^9 \text{ erg cm}^{-3}$ and varied $f_{\text{high-}J}$, ranging from 25% to 100%. The total-to-selective ratio R_V tends to rise with a lower fraction of grains at high- J attractors in the CSE.

$\eta = 0.01$, while it can increase from ~ 1.7 to ~ 2 for grains with $S_{\max} = 10^{10} \text{ erg cm}^{-3}$.

Figure 11 shows the effects of grains at low- J and high- J attractors with $f_{\text{high-}J} = 25\% - 100\%$. We consider these grains have a compact structure with $S_{\max} = 10^9 \text{ erg cm}^{-3}$ located in the envelope with $\eta = 0.002 - 0.01$. The RAT-D efficiency increases with increasing $f_{\text{high-}J}$, causing smaller $R_V < 3.1$ when $f_{\text{high-}J} > 50\%$. By contrast, the GSD of nondisrupted grains at low- J attractors enhances the extinction at optical-IR wavelengths, as shown in Figure 8. Consequently, when $f_{\text{high-}J} < 25\%$, R_V becomes higher and can achieve its maximum up to 4.2 (above the standard value of $R_V \sim 3.1$ in the ISM; see Cardelli et al. 1989).

5.4. Reddening Effects on the Stellar Radiation Spectrum

Figure 12 displays the intrinsic spectrum of Betelgeuse at 3500 K (solid black line). The dashed lines are the radiation spectra accounting for the extinction effect for different values of a_{\max} and without the disruption effect. Since the extinction is higher at shorter wavelengths (i.e., the UV-optical; see Figures 7, 8, and 9), the stellar radiation spectrum is more reddened at the short-wavelength range. In this case, the grain sizes follow a fixed power-law distribution, as described by Equation (13). The level

of reddening depends on the GSD from a_{\min} to a_{\max} . Larger grains present in the envelope for a broader GSD (i.e., a larger maximum grain size a_{\max}), and thus the extinction is strong at UV-NIR wavelengths. Therefore, it significantly reduces the brightness in the UV-NIR photometric bands.

Figure 13 shows the radiation spectra when the RAT-D effect is taken into account (colored lines). Compared with those with no disruption (dashed-dotted black line), the spectra are more enhanced at UV-optical wavelengths.

One important point that we emphasize in Figure 13 is the effect of S_{\max} on the reddened spectra. Compact grains (higher S_{\max}) retain larger sizes in the CSE, while the RAT-D disrupts porous grains (lower S_{\max}). As a consequence, grains with higher S_{\max} attenuate more UV-NIR radiation, while this radiation is less extinguished by grains with lower S_{\max} .

Another crucial point is the major impact of $f_{\text{high-}J}$ on the reddened spectra, as shown in Figure 14. In an environment with a higher fraction of grains at high- J attractors (i.e., high $f_{\text{high-}J}$), the GSD of circumstellar dust is dominated by disrupted grains of $a < a_{\text{disr}}$ (see Figure 5), and extinguishes less UV-NIR radiation. By contrast, for a high fraction of nondisrupted grains at low- J attractors (i.e., low $f_{\text{high-}J}$), large grains remain in their original sizes of $a < a_{\max}$, and the stellar brightness becomes dimmer when observing at UV-NIR regimes.

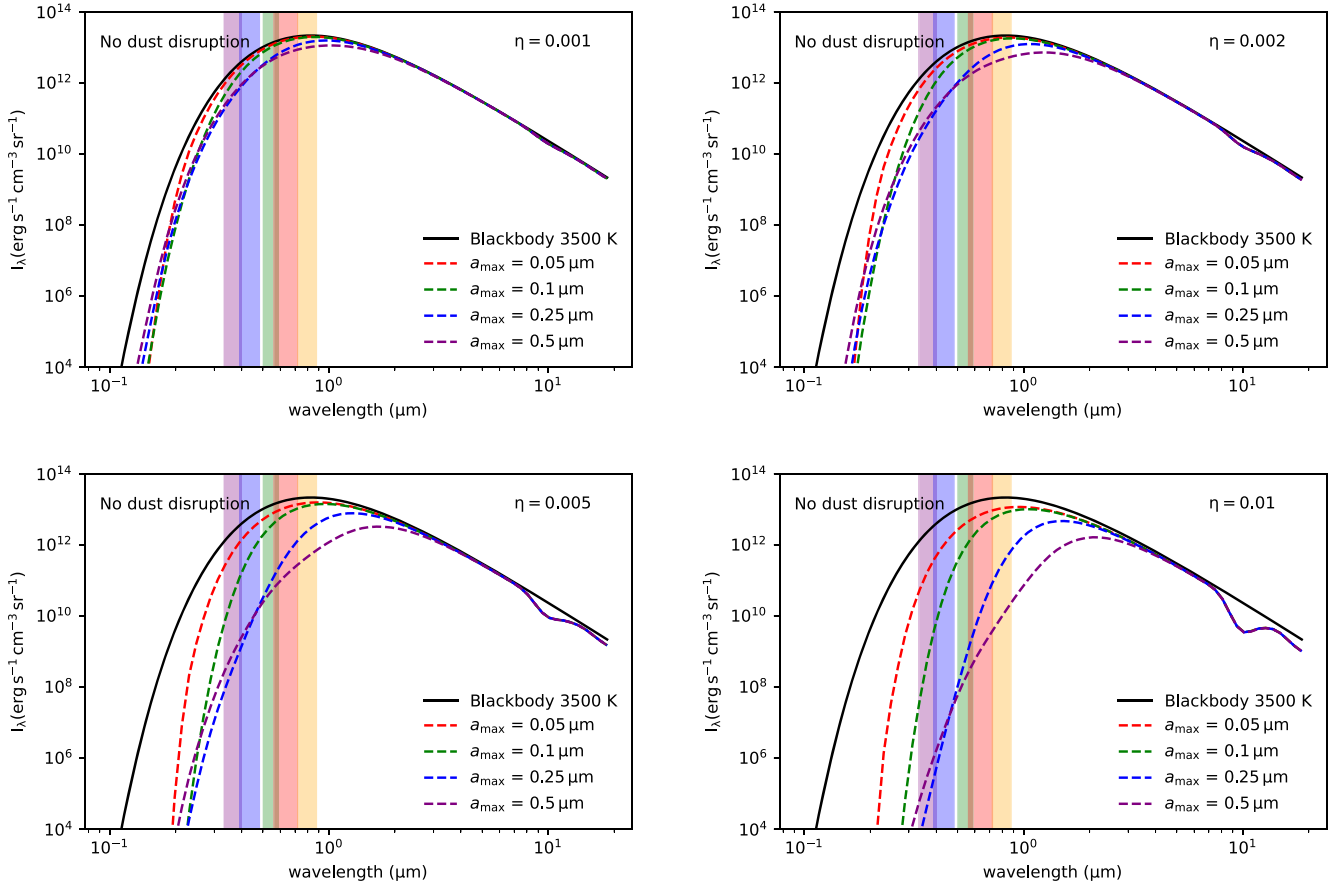


Figure 12. The reddened spectra by CSE dust grains with the variation of a_{\max} without RAT-D (dashed colored lines). Compared with the intrinsic intensity (solid black line), the spectra are more attenuated by large grains from UV to NIR wavelengths. Rectangular boundaries illustrate the photometric bands (see Table 2 in the Appendix B).

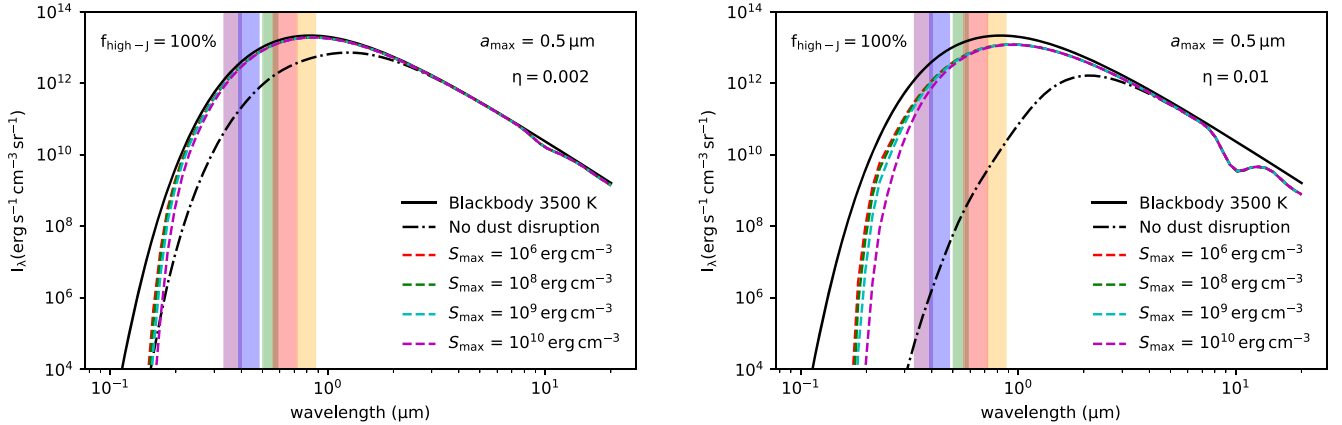


Figure 13. The reddening effects by disrupted grains at various tensile strengths S_{\max} (dashed colored lines). The RAT-D effect can enhance the spectra from UV to NIR wavelengths, compared with the case of no dust disruption with a fixed $a_{\max} = 0.5 \mu\text{m}$ (dashed-dotted black line). The spectra produced by porous grains (i.e., lower S_{\max}) are more enhanced.

Regarding the dust-to-gas ratio, it also influences the distinction of the reddened spectra. For a low dust-to-gas ratio ($\eta \lesssim 0.005$), the extinction effect is weak, and thus the reddened spectra vary slightly. However, for a higher dust-to-gas ratio ($\eta \gtrsim 0.005$), a larger amount of dust reduces the strength of radiation fields, thus diminishing the disruption of grains by RAT-D. Consequently, the discrepancy of the reddened spectra is more significant and is shifted from the UV–optical bands (U , V , and R bands) to the NIR band (I band)

as indicated in Figure 12 for different a_{\max} , in Figure 13 for various S_{\max} , and in Figure 14 for different $f_{\text{high-}j}$.

6. Discussion

In this section, we first mention the use of our model in interpreting GSD in RSG/AGB envelopes, as well as dust extinction and reddening in RSG/AGB observations. Then, we discuss the implications of the results for the observed spectrum of Betelgeuse.

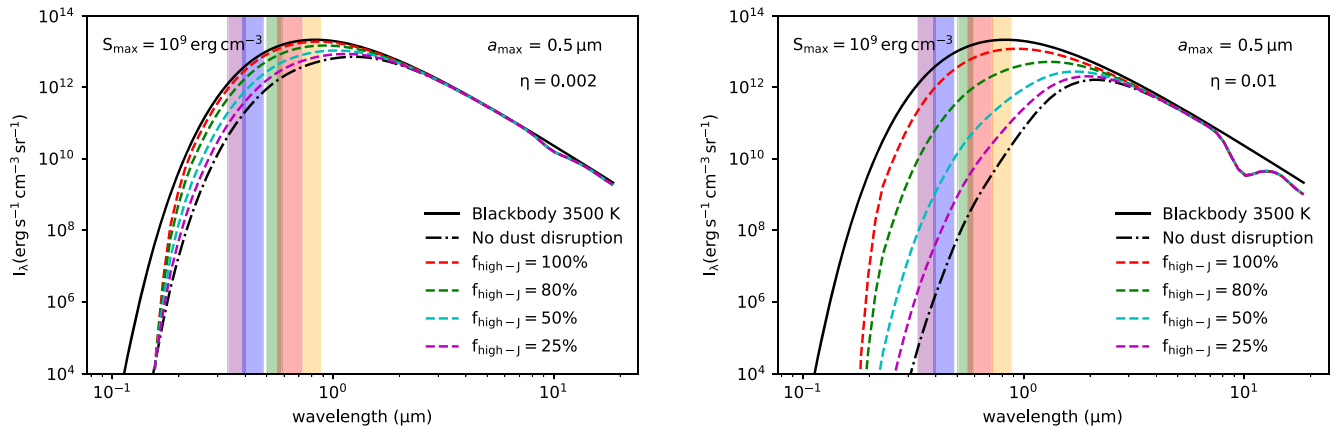


Figure 14. Same as Figure 13 but for a variation of high- J attractors ($f_{\text{high-}J} = 25\%–100\%$). The spectra become redder as the abundance of grains at low- J attractors becomes significantly higher (i.e., lower $f_{\text{high-}J}$).

6.1. Implications for Studying GSD in RSG/AGB Envelopes

The major process driving evolved star outflows is radiation pressure on circumstellar dust in AGB and RSG envelopes (Verhoelst et al. 2006; Höfner 2008; Verhoelst et al. 2009). The modeling results in Figures 4, 5, and 6 imply that, along with translation motion, stellar radiation can induce rotational motion of dust grains and disrupt them by RATs, leading to the abundance of smaller grains of $a < a_{\text{max}} = 0.5 \mu\text{m}$. The variation of GSD can support the understanding of dust formation and evolution in these environments.

RAT-D effects present not only in massive RSGs but also in AGB envelopes, which was previously studied by Tram et al. (2020). The results of GSD in that work showed that stellar radiation can disrupt larger grains into smaller species $a < a_{\text{max}} = 0.25 \mu\text{m}$ at certain regions of both C-rich and O-rich AGB envelopes (see their Figure 3). The authors emphasized that the RAT-D mechanism is independent of grain minerals and can happen for both C-rich dust (e.g., amorphous carbon, SiC, and polycyclic aromatic hydrocarbons) and O-rich dust (e.g., amorphous silicate and crystalline olivine). Thus, rotational disruption by RATs is mainly responsible for modifying the GSD in evolved star envelopes, and should be considered in studies of both RSGs and AGB stars.

Besides, the results of GSD taken by RAT-D are correlated with the chemical modeling results in evolved star envelopes by Van de Sande et al. (2020). The authors showed the potential of retrieving the abundance of smaller grains through higher gas depletion levels due to dust–gas interactions and reactions on the grain surfaces. Hence, the approaches of interpreting depletion levels from molecular line profiles (Van de Sande et al. 2020) and spinning dust emission by RATs (Tram et al. 2020) can help in probing the existence of smaller grains in the CSEs of evolved stars.

6.2. Implications for Dust Extinction and Reddening in RSG/AGB Observations

A previous study by Levesque et al. (2005) described the physical properties of RSGs from broadband filter photometry of 74 Milky Way RSGs. The spectra of these RSGs were estimated by the MARCS models along with the ISM reddening law of Cardelli et al. (1989) with $R_V = 3.1$. The results depicted an excess in the visual magnitude A_V of RSGs

due to the occurrence of circumstellar dust. This dust extinction has also been estimated in the Small Magellanic Cloud, the Large Magellanic Cloud (Levesque et al. 2006), and M31 RSGs (Massey et al. 2009).

The study of Massey et al. (2005) highlighted in more detail the reddening effects of circumstellar dust. Several RSGs demonstrated that the observed fluxes mismatched with the reddened stellar atmospheric models at near-UV (NUV) wavelengths from 0.35 to 0.39 μm (Massey et al. 2005). There are some explanations for this phenomenon. One possibility is the presence of a hot chromosphere above the stellar photosphere. The heating gas profile in the extended atmosphere and strong emissions such as in the Mg II, H α , and K lines are responsible for the rise in UV images and spectra (Gilliland & Dupree 1996; Carpenter et al. 1994; Uitenbroek et al. 1998; Harper et al. 2001). Another explanation is the scattering of blue light from light beams along the LOS by larger grains, as proposed by Massey et al. (2005). These possibilities require high spectral resolution observations. However, it is challenging to extract CSE components for further reddening studies due to high optical depth.

The modeled GSD considering the RAT-D mechanism opens up a new approach in studying dust extinction. The results from Figures 10 and 11 reveal the variation of the observed R_V along the LOS toward background stars as a result of the change in the GSD within the envelope. The measured R_V can achieve up to 4.2, possibly induced by small porous O-rich grains along the LOS across the inner envelope (i.e., $a < 0.05 \mu\text{m}$ and $S_{\text{max}} \sim 10^6 \text{ erg cm}^{-3}$) or the increased population of nondisrupted grains at low- J attractors (i.e., $f_{\text{high-}J} < 25\%$) with larger sizes. This is consistent with $R_V > 3.1$ derived from RSG photometry (Lee 1970; Humphreys 1978). Consequently, the dust extinction determined by RAT-D contributes to correcting photometric observations of RSGs with the modified R_V .

For the NUV problem, there are other explanations with the implication of the RAT-D mechanism. According to the reddening properties in Figures 12, 13, and 14, the NUV excess can be produced by the survival of large grains in stellar radiation fields under the effects of RAT-D. This can be derived from grain properties, from both grain internal structures and rotational properties. One possibility is that grains may have a strong internal structure with

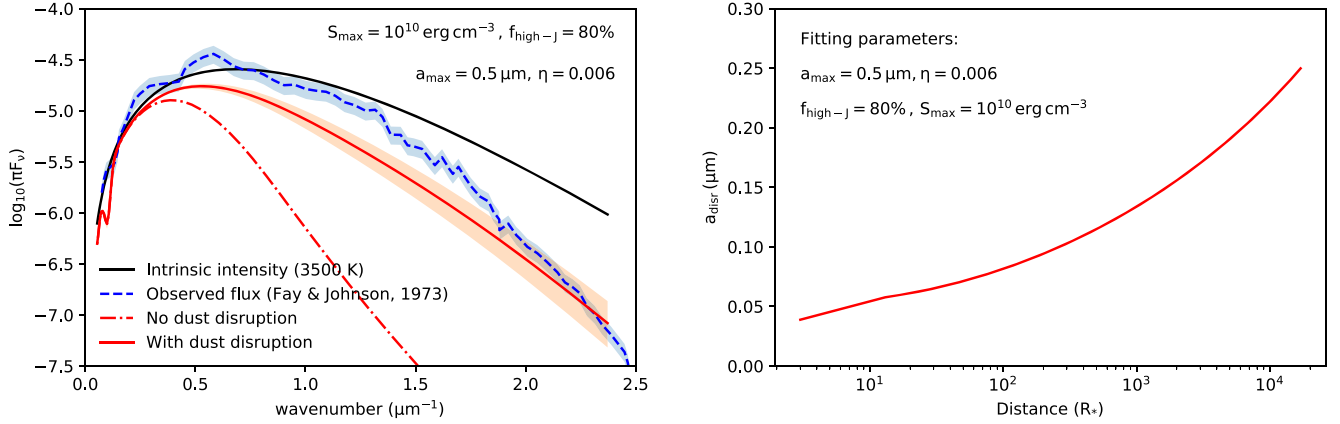


Figure 15. The observed flux of Betelgeuse by Fay & Johnson (1973) (dashed blue line) slightly matched the fitting reddened spectrum considering the RAT-D mechanism (solid red line) within confidence intervals of 1σ for each parameter (red shaded region) in the left panel. The right panel is the grain disruption size given by the grain parameters from the best-fit model.

$S_{\max} > 10^9 \text{ erg cm}^{-3}$, which makes them difficult to disrupt by RATs. This explanation can be reasonable since grains are likely to have a compact structure (e.g., crystalline olivine) at the condensation radius, where the first solids are formed by dust nucleation (see Tielens et al. 1998; Cherchneff 2013; Verhoelst et al. 2009). Another possibility is that grains at low- J attractors may be abundant in RSG envelopes with $f_{\text{high-}J} < 25\%$, requiring a longer disruption timescale (see Figure 5). These suggestions raise the requirement of studying radiative feedback in RSG envelopes to precisely evaluate grain properties from stellar observations.

Circumstellar dust also makes an important impact on interpreting the spectral energy distribution (SED) of AGB stars. Fonfría et al. (2020) and Fonfría et al. (2021) showed that modeling can reproduce the observed SED at a range of wavelengths $\lambda \sim 2.5\text{--}26 \mu\text{m}$. However, their models mismatched and could not reproduce the spectra for shorter wavelengths $\lambda < 2.5 \mu\text{m}$ for both carbon-rich and oxygen-rich AGB stars. Figures 12, 13, and 14 suggest that our model can be a good explanation for these observational puzzles since the RAT-D mechanism applies in both C-rich and O-rich dust as mentioned in Section 6.1. Hence, the effects of RAT-D on circumstellar dust are essential to explaining the extinction at UV–optical wavelengths of AGB envelopes.

6.3. Implications for the Dimming of Betelgeuse

Circumstellar dust affects the observational properties of Betelgeuse, especially its observed flux. The left panel of Figure 15 shows the SED of Betelgeuse observed by Fay & Johnson (1973) (dashed blue line), in comparison with the blackbody radiation at 3500 K (solid black line). The observed flux reveals a strong absorption from the UV to the NIR region at $\gtrsim 0.8 \mu\text{m}^{-1}$. We interpret the circumstellar reddening effects in the observed Betelgeuse spectrum with the application of the RAT-D mechanism.

We first assume that the maximum grain size is equal to $0.5 \mu\text{m}$ (Sciicluna et al. 2015). Thus, the three main free parameters are (1) the maximum tensile strength S_{\max} , (2) the fraction of grains at high- J attractors $f_{\text{high-}J}$, and (3) the dust-to-gas ratio η , which are determined through reduced χ^2

minimization as follows:

$$\chi_{\text{red}}^2 = \frac{1}{L} \sum_{i=1}^n \frac{(y_i - \bar{y}_i)^2}{\sigma_i^2} \quad (21)$$

where L is the number of freedom degrees, n is the number of data points, y_i and \bar{y}_i are the observed and modeling values, respectively, and σ_i is the measurement error of the observed flux. We test the effect of assuming flux errors on the minimum χ_{red}^2 .

The best model is illustrated by the solid red line in Figure 15 (left panel) with $S_{\max} = 10^{10} \text{ erg cm}^{-3}$, $f_{\text{high-}J} = 80\%$, and a dust-to-gas ratio $\eta = 0.006$ within a 1σ level of significance (red shaded region), assuming a 20% error of the total flux (blue shaded region). These parameters change negligibly when we vary the error from 5% to 30%. The constrained dust-to-gas ratio is higher than that of 0.0025 predicted by Verhoelst et al. (2006). The fitted S_{\max} and $f_{\text{high-}J}$ imply that approximately 80% of the original large grains at high- J attractors may obtain compact structures before being fragmented by RAT-D. We compare our best fit with the case of no RAT-D, which is shown by a dashed–dotted red line. This standard case considerably underestimates the observed flux at optical and UV wavelengths due to a lack of small grains.

From the best fit, we compute the change in the GSD of disrupted grains as a function of the envelope distance, which is shown in the right panel of Figure 15. The grain size varies from $\sim 0.05 \mu\text{m}$ at $r = 3 R_*$ to $\sim 0.25 \mu\text{m}$ at $r = 17,000 R_*$, which is apparently higher than the mean grain size of the ISM of $0.1 \mu\text{m}$ (Cardelli et al. 1989).

The results found in Figure 15 illustrate the scenario of driving outflows by two populations of grains at high- J and low- J attractors based on the differences in dust–gas drift velocity. The former shows the dominance of smaller grains (i.e., $a \lesssim 0.1 \mu\text{m}$) induced by RAT-D at the dust formation zone, which are expelled more easily due to the radiation pressure. These grains subsequently collide with gas molecules and move at subsonic speed (see Section 2.5 in Tram et al. 2020). The latter shows the survival of large grains (i.e., $a \gtrsim 0.1 \mu\text{m}$) due to a longer disruption timescale, which produces higher drift velocity and can achieve supersonic speed (Tram et al. 2020). Consequently, RAT-D plays a

significant role in defining grain properties and their dependency on radiation fields to push materials into the ISM environment.

However, the left panel in Figure 15 shows a slight deviation between the modeled SED and the observed spectrum at optical–NIR wavelengths. There are several factors that may contribute to this difference. One factor could be the impacts of the gaseous atmosphere, which can be caused by strong absorption lines of heavy metal species (e.g., TiO and CN; see Fay & Johnson 1973; Tsuji 1976; Lobel 2002) or the emission by heating gas at the chromosphere region at the optical–UV regimes (see Lim et al. 1998; Harper et al. 2001). Another factor might be the presence of dense clumps due to a local cooling, contributing to 3%–12% of the total mass loss of Betelgeuse (Montargès et al. 2021). Unlike the continuous envelope considered in this work, the clumpy structure is expected to cause less extinction, which could improve our model’s interpretations.

6.4. Model Limitations

This work is our first attempt to describe dust properties and their impacts on stellar observations in the presence of RAT-D from massive RSGs. Therefore, our model exhibits some limitations, which are emphasized in this section.

First, our study adopts a simplified assumption on the spherical geometry of the Betelgeuse envelope produced by radiation pressure on dust grains (see Figure 2). This differs from the asymmetric structures with dense clumps in recent optical–NIR observations (e.g., Kervella et al. 2011; Ohnaka 2014; Montargès et al. 2021), which can be a result of mass ejection by large-scale convection in the stellar surface (Freytag et al. 2002; Ren & Jiang 2020; Humphreys & Jones 2022). As extensively studied in Giang et al. (2021), a high concentration of gas inside clumps can enhance rotational damping by gas collision with a shorter timescale (see Equation (10)) and reduce the RAT-D efficiency. This can probe the occurrence of large grains of $a > 0.1 \mu\text{m}$ found in the dusty clump of Betelgeuse and other RSGs (Sciuluna et al. 2015; Cannon et al. 2021; Montargès et al. 2021).

Second, we consider the stellar emission as blackbody radiation for the sake of simplicity. The model disregards the contribution of a complex stellar atmosphere at optical–UV wavelengths, as we describe in Figure 15 for the SED fitting. These factors can improve the model with best-fit parameters and help in interpreting deeper dust properties with various environmental conditions of the evolved star envelopes.

Despite these limitations, we believe that consideration of the RAT-D mechanism is essential in modeling radiative feedback on circumstellar dust, and can provide a proper insight to understand grain formation and evolution and their effects on AGB/RSG observations.

7. Summary

This paper focuses on modeling the effects of rotational disruption of circumstellar dust by RATs and exploring its impact on photometric and spectroscopic observations of RSG and AGB stars. The main findings of our study are summarized as follows.

1. Assuming that large grains can form in the dust formation zone, we find that the RAT-D mechanism can destroy large grains and enhance smaller grains of $a_{\text{disr}} < a_{\text{max}}$.

The mechanism can result in the modification of the GSD with envelope distance, depending on both grain properties (i.e., sizes, internal structures, and rotational properties) and environmental properties (i.e., dust-to-gas mass ratio).

2. With the GSD determined by RAT-D, we model the dust extinction along the sightline toward Betelgeuse and background stars. The steepness of the extinction curve is related to the grain properties and the projected distance of the LOS in the CSE.
3. We calculate the variation of the total-to-selective extinction ratio R_V . The change in R_V correlates with the change in the slope of the observed extinction due to the modification of the GSD constrained by RAT-D.
4. We study the circumstellar dust reddening effects of Betelgeuse. The observed stellar spectrum in UV–NIR regions is enhanced as compared with the case without dust disruption. Grain and environmental properties modify the reddening level.
5. The effects of the RAT-D mechanism can be applied in studying the extinction and reddening of AGB/RSG stars, especially for interpreting the NUV excess in the SEDs of RSGs. Thus, the RAT-D mechanism should be considered in studies of the dusty envelopes around RSG and AGB stars.
6. The effects of the RAT-D mechanism potentially contribute to the probing of the spectral flux of Betelgeuse observed by Fay & Johnson (1973). We find that radiation-driven winds can be generated by both small grains at high- J attractors and large grains at low- J attractors with different dust–gas drift velocities.
7. The properties of the gaseous atmosphere and clumpy structures in the Betelgeuse envelope possibly affect the dust reddening and disruption. Detailed calculations with more realistic characteristics of RSG envelopes are required to investigate precisely the impacts of radiative feedback and constrain proper circumstellar dust properties through stellar observations.

We thank the anonymous referee for helpful comments that improved the impact and the presentation of this paper. T.H. acknowledges support from a National Research Foundation of Korea grant (2019R1A2C1087045) funded by the Korean government (MSIT). This work was partly supported by a grant from the Simons Foundation (916424, N.H.). We would like to thank the ICISE staff for their enthusiastic support. Bao Truong acknowledges the support from the Simons Astrophysics Group at ICISE (SAGI) for a summer internship. This research was done in the framework of the Vietnam Astrophysics Research NETWORK (VARNET), which aims to foster collaborative research in astrophysics among Vietnamese researchers and students living in Vietnam and abroad.

Appendix A

Extinction per Column Density A_λ/N_H

Figure 16 shows the normalized extinction curve A_λ/N_H , where $N_H = \int n_H ds$ is the hydrogen column density along the LOS with two cases: $z = 0$ (from Betelgeuse) and $z \neq 0$ (from a background star). One can see that the visual extinction A_V at $\lambda = 0.5448$ increases with increasing S_{max} , which was used for modifying the observed extinction curve A_λ/A_V in Section 5.2.

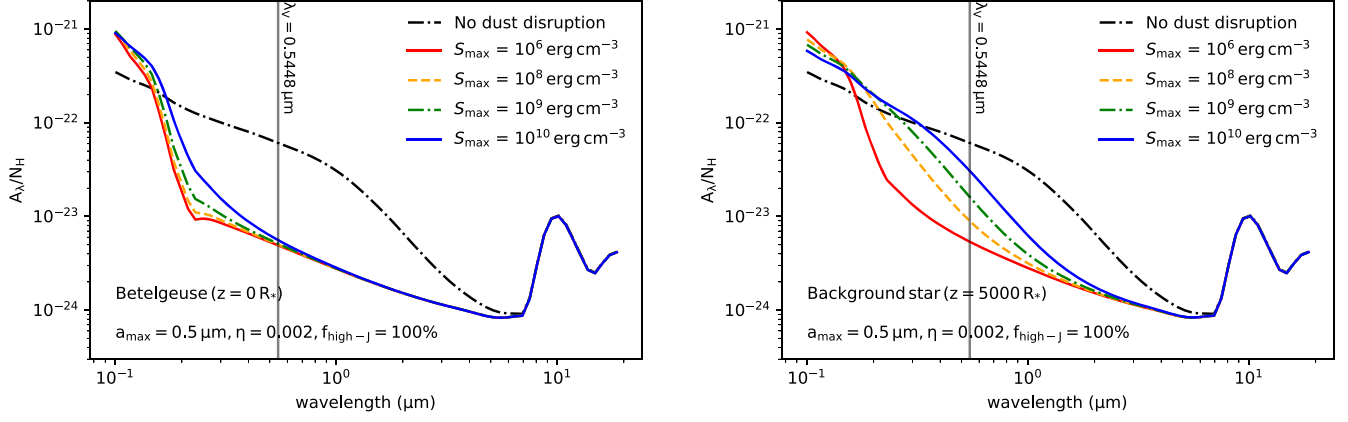


Figure 16. Extinction curve A_λ/N_H caused by dust grains along an LOS at $z = 0 R_*$ (through Betelgeuse, left panel) and $z = 500 R_*$ (through a background star, right panel) at different values of S_{\max} with a fixed $a_{\max} = 0.5 \mu\text{m}$ and $f_{\text{high-}J} = 100\%$. The vertical line represents the visual extinction A_V at $\lambda = 0.5448 \mu\text{m}$.

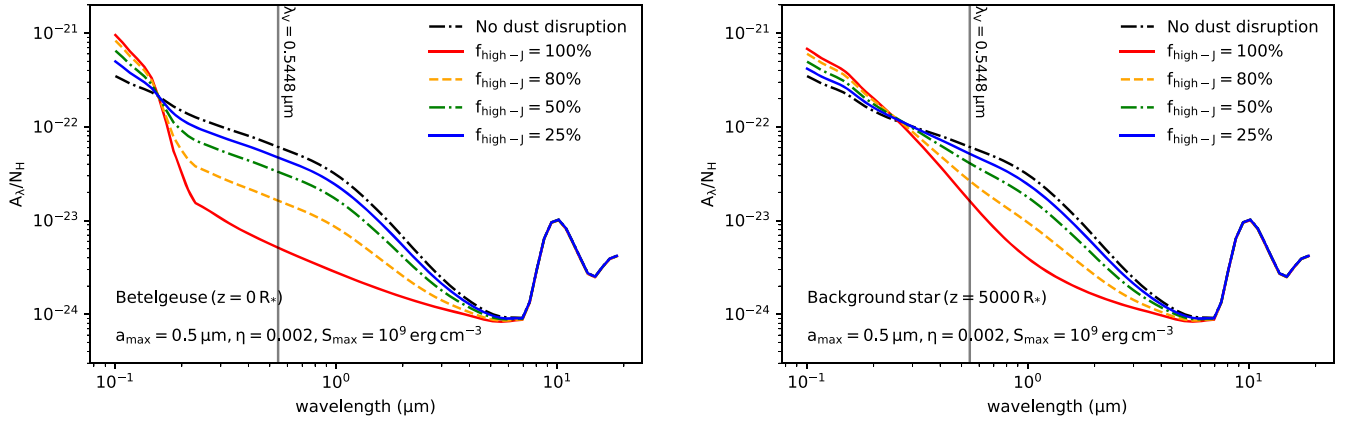


Figure 17. Same as Figure 16 but for various values of $f_{\text{high-}J}$ from 25% to 100%, assuming a fixed $S_{\max} = 10^9 \text{ erg cm}^{-3}$ and $\eta = 0.002$.

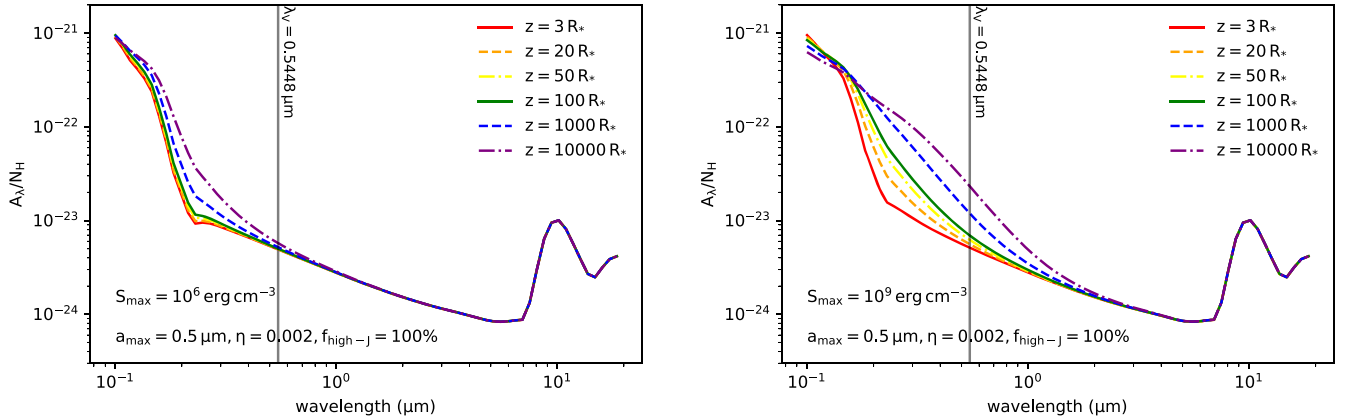


Figure 18. Same as Figure 16 but for different positions z along the LOS. We consider dust grains with $S_{\max} = 10^6 \text{ erg cm}^{-3}$ (left panel) and $S_{\max} = 10^9 \text{ erg cm}^{-3}$ (right panel).

Similar to Figure 7, the figure shows an increase in optical–IR extinction and a decrease in far-UV extinction for grains with higher S_{\max} , and the extinction in the right panel exhibits a flatter slope than that in the left panel.

Figure 17 indicates the change in the extinction curve A_λ/N_H with different values of the fraction $f_{\text{high-}J}$ of grains at high- J attractors between two cases of the LOS $z = 0$ and $z \neq 0$ (considering a fixed S_{\max}). As in Figure 8, the increased

contribution of disrupted grain sizes (i.e., higher $f_{\text{high-}J}$) leads to a higher far-UV extinction and a lower optical–IR extinction. The value of A_V increases with decreasing $f_{\text{high-}J}$.

Figure 18 reveals an increase in the extinction curve A_λ/N_H at higher positions z of a parallel LOS due to the survival of larger grains caused by RAT-D, as also shown in Figure 9. The visual extinction A_V is higher for larger z .

Appendix B











The *UBVRI* Photometric System

Table 2 describes the photometric bands from ultraviolet to infrared in the *UBVRI* system, which were calibrated and corrected by Bessell (1990). The marked colors and bandwidths $\Delta\lambda$ are used for setting the rectangular boundaries in Figures 12, 13, and 14.

Table 2
The *UBVRI* Photometric System (Bessell 1990, 2005)

Photometric Band	Effective Wavelength λ_{eff} (μm)	Bandwidth $\Delta\lambda$ (μm)	Marked Color
<i>U</i>	0.3659	0.065	Purple
<i>B</i>	0.4363	0.089	Blue
<i>V</i>	0.5448	0.084	Green
<i>R</i>	0.6407	0.158	Red
<i>I</i>	0.7982	0.154	Orange

ORCID iDs

Bao Truong  <https://orcid.org/0000-0001-9654-8051>
 Le Ngoc Tram  <https://orcid.org/0000-0002-6488-8227>
 Thiem Hoang  <https://orcid.org/0000-0003-2017-0982>
 Nguyen Chau Giang  <https://orcid.org/0000-0002-3681-671X>
 Pham Ngoc Diep  <https://orcid.org/0000-0002-2808-0888>
 Dieu D. Nguyen  <https://orcid.org/0000-0002-5678-1008>
 Thuong D. Hoang  <https://orcid.org/0000-0002-3437-5228>
 Nguyen Bich Ngoc  <https://orcid.org/0000-0002-5913-5554>
 Nguyen Fuda  <https://orcid.org/0000-0002-6372-839>
 Hien Phan  <https://orcid.org/0000-0003-4935-462X>

References

- Antia, H. M., Chitre, S. M., & Narasimha, D. 1984, *ApJ*, 282, 574
 Bennett, P. D. 2010, in ASP Conf. Ser. 425, Hot and Cool: Bridging Gaps in Massive Star Evolution, ed. C. Leitherer, P. D. Bennett, P. W. Morris, & J. T. Van Loon (San Francisco, CA: ASP), 181
 Bessell, M. S. 1990, *PASP*, 102, 1181
 Bessell, M. S. 2005, *ARA&A*, 43, 293
 Biscaro, C., & Cherneteff, I. 2016, *A&A*, 589, A132
 Cannon, E., Montargès, M., de Koter, A., et al. 2021, *MNRAS*, 502, 369
 Cardelli, J. A., Clayton, G. C., & Mathis, J. S. 1989, *ApJ*, 345, 245
 Carpenter, K. G., Robinson, R. D., Wahlgren, G. M., Linsky, J. L., & Brown, A. 1994, *ApJ*, 428, 329
 Cherneteff, I. 2013, in EAS Publications Ser. 60, Betelgeuse Workshop 2012, ed. P. Kervella, T. Le Bertre, & G. Perrin (Les Ulis: EDP), 175
 De Beck, E., Boyer, M. L., Bujarrabal, V., et al. 2019, *BAAS*, 51, 374
 Decin, L., Cox, N. L. J., Royer, P., van Marle, A. J., & Vandebussche, B. 2013, in EAS Publications Ser. 60, Betelgeuse Workshop 2012, ed. P. Kervella, T. Le Bertre, & G. Perrin (Les Ulis: EDP), 227
 Dolan, M. M., Mathews, G. J., Lam, D. D., et al. 2016, *ApJ*, 819, 7
 Dominik, C., Gail, H. P., & Sedlmayr, E. 1989, *A&A*, 223, 227
 Draine, B. T. 2011, *Physics of the Interstellar and Intergalactic Medium* (Princeton, NJ: Princeton Univ. Press)
 Draine, B. T., & Flatau, P. J. 2012, arXiv:1202.3424
 Draine, B. T., & Lee, H. M. 1984, *ApJ*, 285, 89
 Draine, B. T., & Salpeter, E. E. 1979, *ApJ*, 231, 77
 Fadeyev, Y. A. 2012, *AsTL*, 38, 260
 Fay, T. D., & Johnson, H. R. 1973, *ApJ*, 181, 851
 Fonfría, J. P., Montiel, E. J., Cernicharo, J., et al. 2021, *A&A*, 651, A8
 Fonfría, J. P., Montiel, E. J., Cernicharo, J., DeWitt, C. N., & Richter, M. J. 2020, *A&A*, 643, L15
 Freytag, B., Steffen, M., & Dorch, B. 2002, *AN*, 323, 213
 Giang, N. C., & Hoang, T. 2021, *ApJ*, 922, 47
 Giang, N. C., Hoang, T., Tram, L. N., et al. 2021, arXiv:2111.11800
 Giang, N. C., Hoang, T., & Tram, L. N. 2020, *ApJ*, 888, 93
 Gilliland, R. L., & Dupree, A. K. 1996, *ApJL*, 463, L29
 Glassgold, A. E., & Huggins, P. J. 1986, *ApJ*, 306, 605
 Goldberg, L. 1984, *PASP*, 96, 366
 Greenberg, J. M., & Li, A. 1996, *A&A*, 309, 258
 Groenewegen, M. A. T., Sloan, G. C., Soszyński, I., & Petersen, E. A. 2009, *A&A*, 506, 1277
 Groh, J. H., Meynet, G., Georgy, C., & Ekström, S. 2013, *A&A*, 558, A131
 Guo, J. H., & Li, Y. 2002, *ApJ*, 565, 559
 Harper, G. M., Brown, A., & Lim, J. 2001, *ApJ*, 551, 1073
 Hartmann, L., & Avrett, E. H. 1984, *ApJ*, 284, 238
 Heger, A., Jeannin, L., Langer, N., & Baraffe, I. 1997, *A&A*, 327, 224
 Herranen, J., Lazarian, A., & Hoang, T. 2021, *ApJ*, 913, 63
 Hirashita, H., & Voshchinnikov, N. V. 2014, *MNRAS*, 437, 1636
 Hoang, T., Lazarian, A., & Martin, P. G. 2013, *ApJ*, 779, 152
 Hoang, T., Tram, L. N., Lee, H., & Ahn, S.-H. 2019, *NatAs*, 3, 766
 Hoang, T., Tram, L. N., Lee, H., Diep, P. N., & Ngoc, N. B. 2021, *ApJ*, 908, 218
 Höfner, S. 2008, *A&A*, 491, L1
 Höfner, S. 2009, in ASP Conf. Ser. 414, Cosmic Dust—Near and Far, ed. T. Henning, E. Grün, & J. Steinacker (San Francisco, CA: ASP), 3
 Höfner, S., Bladh, S., Aringer, B., & Ahuja, R. 2016, *A&A*, 594, A108
 Höfner, S., & Olofsson, H. 2018, *A&A Rv*, 26, 1
 Humphreys, R. M. 1978, *ApJS*, 38, 309
 Humphreys, R. M., & Jones, T. J. 2022, *AJ*, 163, 103
 Kervella, P., Lagadec, E., Montargès, M., et al. 2016, *A&A*, 585, A28
 Kervella, P., Perrin, G., Chiavassa, A., et al. 2011, *A&A*, 531, A117
 Kilpatrick, C. D., & Foley, R. J. 2018, *MNRAS*, 481, 2536
 Kiss, L. L., Szabó, G. M., & Bedding, T. R. 2006, *MNRAS*, 372, 1721
 Kochanek, C. S., Khan, R., & Dai, X. 2012, *ApJ*, 759, 20
 Laor, A., & Draine, B. T. 1993, *ApJ*, 402, 441
 Lazarian, A., & Hoang, T. 2007, *MNRAS*, 378, 910
 Lazarian, A., & Hoang, T. 2021, *ApJ*, 908, 12
 Lee, T. A. 1970, *ApJ*, 162, 217
 Levesque, E. M., Massey, P., Olsen, K. A. G., et al. 2005, *ApJ*, 628, 973
 Levesque, E. M., Massey, P., Olsen, K. A. G., et al. 2006, *ApJ*, 645, 1102
 Lim, J., Carilli, C. L., White, S. M., Beasley, A. J., & Marson, R. G. 1998, *Natur*, 392, 575
 Lobel, A. 2002, The 12th Cambridge Workshop on Cool Stars, Stellar Systems, and the Sun, arXiv:astro-ph/0211506
 Lovegrove, E., & Woosley, S. E. 2013, *ApJ*, 769, 109
 Massey, P., Plez, B., Levesque, E. M., et al. 2005, *ApJ*, 634, 1286
 Massey, P., Silva, D. R., Levesque, E. M., et al. 2009, *ApJ*, 703, 420
 Mathis, J. S., Mezger, P. G., & Panagia, N. 1983, *A&A*, 500, 259
 Mathis, J. S., Rimpl, W., & Nordsieck, K. H. 1977, *ApJ*, 217, 425
 Meynet, G., & Maeder, A. 2003, *A&A*, 404, 975
 Montargès, M., Cannon, E., Lagadec, E., et al. 2021, *Natur*, 594, 365
 Nataf, D. M., Gonzalez, O. A., Casagrande, L., et al. 2016, *MNRAS*, 456, 2692
 Noriega-Crespo, A., van Buren, D., Cao, Y., & Dgani, R. 1997, *AJ*, 114, 837
 O’Gorman, E., Harper, G. M., Brown, A., et al. 2015, *A&A*, 580, A101
 Ohnaka, K. 2014, *A&A*, 568, A17
 Pijpers, F. P., & Hearn, A. G. 1989, *A&A*, 209, 198
 Ren, Y., & Jiang, B.-W. 2020, *ApJ*, 898, 24
 Rodgers, B., & Glassgold, A. E. 1991, *ApJ*, 382, 606
 Schwarzschild, M. 1975, *ApJ*, 195, 137
 Scicluna, P., Siebenmorgen, R., Wesson, R., et al. 2015, *A&A*, 584, L10
 Seab, C. G., & Snow, T. P. 1989, *ApJ*, 347, 479
 Smartt, S. J., Eldridge, J. J., Crockett, R. M., & Maund, J. R. 2009, *MNRAS*, 395, 1409
 Tielens, A. G. G. M. 1983, *ApJ*, 271, 702
 Tielens, A. G. G. M., Waters, L. B. F. M., & Bernatowicz, T. J. 2005, in ASP Conf. Ser. 341, Chondrites and the Protoplanetary Disk, ed. A. N. Krot, E. R. D. Scott, & B. Reipurth (San Francisco, CA: ASP), 605
 Tielens, A. G. G. M., Waters, L. B. F. M., Molster, F. J., & Justtanont, K. 1998, *Ap&SS*, 255, 415
 Tram, L. N., Hoang, T., Soam, A., Lesaffre, P., & Reach, W. T. 2020, *ApJ*, 893, 138
 Tsuji, T. 1976, *PASJ*, 28, 567
 Uitenbroek, H., Dupree, A. K., & Gilliland, R. L. 1998, *AJ*, 116, 2501
 Van de Sande, M., Walsh, C., & Danilovich, T. 2020, *MNRAS*, 495, 1650
 van Loon, J. T., Cioni, M. R. L., Zijlstra, A. A., & Loup, C. 2005, *A&A*, 438, 273
 Verhoelst, T., Decin, L., van Malderen, R., et al. 2006, *A&A*, 447, 311
 Verhoelst, T., van der Zypen, N., Hony, S., et al. 2009, *A&A*, 498, 127
 Walmswell, J. J., & Eldridge, J. J. 2012, *MNRAS*, 419, 2054
 Woosley, S. E., & Heger, A. 2012, *ApJ*, 752, 32
 Yoon, S.-C., & Cantiello, M. 2010, *ApJL*, 717, L62